

Proceedings of the Institution of Mechanical Engineers, Part L: Journal of Materials Design and Applications

<http://pil.sagepub.com/>

Effect of the tin- versus air-side plate-glass orientation on the impact response and penetration resistance of a laminated transparent armour structure

M Grujicic, W C Bell, B Pandurangan, B A Cheeseman, P Patel and P G Dehmer

Proceedings of the Institution of Mechanical Engineers, Part L: Journal of Materials Design and Applications 2012 226:

119 originally published online 16 January 2012

DOI: 10.1177/1464420711433991

The online version of this article can be found at:

<http://pil.sagepub.com/content/226/2/119>

Published by:



<http://www.sagepublications.com>

On behalf of:



[Institution of Mechanical Engineers](http://www.imechE.org)

Additional services and information for *Proceedings of the Institution of Mechanical Engineers, Part L: Journal of Materials Design and Applications* can be found at:

Email Alerts: <http://pil.sagepub.com/cgi/alerts>

Subscriptions: <http://pil.sagepub.com/subscriptions>

Reprints: <http://www.sagepub.com/journalsReprints.nav>

Permissions: <http://www.sagepub.com/journalsPermissions.nav>

Citations: <http://pil.sagepub.com/content/226/2/119.refs.html>

>> [Version of Record](#) - Mar 12, 2012

[OnlineFirst Version of Record](#) - Jan 16, 2012

[What is This?](#)

Report Documentation Page

Form Approved
OMB No. 0704-0188

Public reporting burden for the collection of information is estimated to average 1 hour per response, including the time for reviewing instructions, searching existing data sources, gathering and maintaining the data needed, and completing and reviewing the collection of information. Send comments regarding this burden estimate or any other aspect of this collection of information, including suggestions for reducing this burden, to Washington Headquarters Services, Directorate for Information Operations and Reports, 1215 Jefferson Davis Highway, Suite 1204, Arlington VA 22202-4302. Respondents should be aware that notwithstanding any other provision of law, no person shall be subject to a penalty for failing to comply with a collection of information if it does not display a currently valid OMB control number.

1. REPORT DATE JAN 2012		2. REPORT TYPE		3. DATES COVERED 00-00-2012 to 00-00-2012	
4. TITLE AND SUBTITLE Effect of the tin- versus air-side plate-glass orientation on the impact response and penetration resistance of a laminated transparent armour structure				5a. CONTRACT NUMBER	
				5b. GRANT NUMBER	
				5c. PROGRAM ELEMENT NUMBER	
6. AUTHOR(S)				5d. PROJECT NUMBER	
				5e. TASK NUMBER	
				5f. WORK UNIT NUMBER	
7. PERFORMING ORGANIZATION NAME(S) AND ADDRESS(ES) Clemson University, Department of Mechanical Engineering, 241 Engineering Innovation Building, Clemson, SC, 29634				8. PERFORMING ORGANIZATION REPORT NUMBER	
9. SPONSORING/MONITORING AGENCY NAME(S) AND ADDRESS(ES)				10. SPONSOR/MONITOR'S ACRONYM(S)	
				11. SPONSOR/MONITOR'S REPORT NUMBER(S)	
12. DISTRIBUTION/AVAILABILITY STATEMENT Approved for public release; distribution unlimited					
13. SUPPLEMENTARY NOTES					
14. ABSTRACT Our recently developed continuum-level, physically based, high strain-rate, large strain high-pressure mechanical material model for soda-lime glass has been enhanced to include differences in the flaw-size population between the so-called air-side and the so-called tin-side of float-glass plates, and adapted for use in the case of borosilicate glass. The model was structured in such a way that it is suitable for direct incorporation, as a material user-subroutine, into standard commercial transient non-linear dynamics finite-element-based software packages. The model was parameterized using various open-literature sources. The experimental portion of the work, which consisted of 28 projectile impacts onto glass/polyurethane/ polycarbonate-based test laminates, was intended to allow for quantification of the effect of air- versus tin-side borofloat strike surface when incorporated into a multi-layer, multi-functional test laminate. Experimental findings indicated the lack of a significant difference in the impact resistance of air- versus tin-side test laminate strike surfaces. Subsequent to these findings computational simulations were carried out in order to establish if the proposed borofloat material model could capture the prominent experimentally observed damage modes and the measured V50, reconfirming the experimental findings. In general, a good agreement was found between the computational and the experimental results.					
15. SUBJECT TERMS					
16. SECURITY CLASSIFICATION OF:			17. LIMITATION OF ABSTRACT Same as Report (SAR)	18. NUMBER OF PAGES 26	19a. NAME OF RESPONSIBLE PERSON
a. REPORT unclassified	b. ABSTRACT unclassified	c. THIS PAGE unclassified			

Effect of the tin- versus air-side plate-glass orientation on the impact response and penetration resistance of a laminated transparent armour structure

M Grujic^{1*}, W C Bell¹, B Pandurangan¹, B A Cheeseman², P Patel², and P G Dehmer²

¹Department of Mechanical Engineering, Clemson University, Clemson, South Carolina, USA

²Survivability Materials Branch, Army Research Laboratory, Aberdeen Proving Ground, Maryland, USA

The manuscript was received on 3 June 2011 and was accepted after revision for publication on 28 October 2011.

DOI: 10.1177/1464420711433991

Abstract: Our recently developed continuum-level, physically based, high strain-rate, large-strain, high-pressure mechanical material model for soda-lime glass has been enhanced to include differences in the flaw-size population between the so-called *air-side* and the so called *tin-side* of float-glass plates, and adapted for use in the case of borosilicate glass.

The model was structured in such a way that it is suitable for direct incorporation, as a material user-subroutine, into standard commercial transient non-linear dynamics finite-element-based software packages. The model was parameterized using various open-literature sources. The experimental portion of the work, which consisted of 28 projectile impacts onto glass/polyurethane/polycarbonate-based test laminates, was intended to allow for quantification of the effect of air- versus tin-side borofloat strike surface when incorporated into a multi-layer, multi-functional test laminate. Experimental findings indicated the lack of a significant difference in the impact resistance of air- versus tin-side test laminate strike surfaces. Subsequent to these findings, computational simulations were carried out in order to establish if the proposed borofloat material model could capture the prominent experimentally observed damage modes and the measured V50, reconfirming the experimental findings. In general, a good agreement was found between the computational and the experimental results.

Keywords: Borofloat[®] glass, material modelling, impact resistance, tin-side versus air-side

1 INTRODUCTION

Impact-resistant glass is a material (or more often a system of materials) designed to be optically transparent while providing the necessary level of protection against high-rate loading (e.g. those associated with storm winds, blasts, high-speed fragments and projectiles, etc.). This class of materials is used in such diverse applications as storm windows, automobile windshields, bullet-resistant windows, protective visors for non-combat usage (e.g. riot control or

explosive ordinance disposal) or as transparent armour systems (to protect on-board instruments/sensors from fragments and debris, and to protect vehicle occupants from terrorist actions or other hostile events). The continued push for advancement in the development and application of impact-resistant glass is chiefly the result of the ever-increasing need of the military for more mass-efficient transparent materials. This need is associated with continuing escalations in the number and variety of threats and the desire of the military to become more mobile, deployable, and sustainable.

Traditionally, protective transparent structures (or systems) used in military applications are constructed of monolithic glass or transparent-elastomer inter-layered glass laminates. Among the new

*Corresponding author: Department of Mechanical Engineering, Clemson University, 241 Engineering Innovation Building, Clemson, SC 29634-0921, USA.
email: gmica@clemson.edu

transparent armour materials and technologies available today, the following have received the most attention: crystalline ceramics (e.g. aluminium-oxy-nitride spinel, AlON [1]), new transparent polymer materials (e.g. transparent nylon [2]), and new inter-layer technologies (e.g. polyurethane bonding layers [1]), and new laminate designs [3]. Due to the large size and complex shapes of most protective transparent structures in military applications, the structures are still predominantly based on glass. In other words, while ever-increasing demands for reductions in weight and for improvements in impact-resistance of protective transparent structures are calling for increased use of the aforementioned new transparent materials and advanced structures, glass (as well as glass ceramics) continues to remain the material of choice (especially in military ground-vehicle applications). The main reasons for the continued use of glass as the dominate transparent armour constituent material are as follows.

1. Compositional modifications, chemical strengthening, and controlled crystallization have demonstrated to be capable of significantly improving the impact resistance of glass [3].
2. Glass windshields and windows can also be produced in large sizes with curved geometries, and can be fabricated to provide an incremental improvement in impact resistance at an incremental cost.

The development of new glass-based protective transparent structures with improved mass-normalized impact resistance typically includes extensive experimental test programs. Such experimental test programs are critical for ensuring the utility and effectiveness of the protective transparent structures. However, the use of experimental test programs is generally expensive, time-consuming, and involves destructive testing. While the role of experimental test programs remains critical, they are increasingly being complemented by the corresponding computation-based engineering analyses and simulations. Knowledge of the constituent transparent materials' response under high-deformation rate/high-pressure loading conditions, as described by the corresponding material model, is one of the key components in such analyses greatly affecting their utility and fidelity. In addition, it is imperative to understand the individual and combined effects of the constituent material layers in multi-layer protective transparent structures. The main objective of this study is to help advance the use of these computational engineering analyses and simulations in protective transparent structure design applications by further developing the physically based material model for soda-lime

ballistic glass (developed in references [4, 5]). Specifically, the new rendition of the glass material model is extended to other glass formulations (in particular to the borosilicate float glass, Borofloat[®] glass) and enhanced to account for the effect of micro-structural/compositional differences between the so-called *air-side* and the so-called *tin-side* of plate glass fabricated using a conventional float-glass process. It should be noted that borosilicate glass was experimentally and computationally investigated in this study not in the form of monolithic, single-constituent test structures, but rather as a lamina in a borosilicate/polyurethane/polycarbonate test laminate (a basic laminated transparent armour repeat unit). The main reason for this approach is that the contribution of a lamina to the laminate performance is affected not only by the material response of the lamina in question (the local effect), but also by the interactions of this lamina with the surrounding laminae/structures (the system-level effect).

It is well established that the ability of glass (as is also the case with the majority of brittle materials) to support external loading is controlled by size and morphology distribution of pre-existing flaws and that this ability is considerably lower in the case of externally applied tensile/bending loads [6, 7]. Consequently, the observed strength of glass is typically found to be only a minor fraction of its theoretical strength. While flaws are present throughout the entire volume of a glass structure (e.g. plate glass), it is generally recognized that a flaw distribution of higher number density and increased potency is associated with the structure surfaces [6, 7]. Consequently, when plate glass is subjected to bending (typically mode I) cracks nucleate at pre-existing flaws on the plate-glass surface which are subject to tensile loads. Nucleated cracks continue to propagate through the plate-glass thickness (and along its surface) as the loading is increased and will ultimately lead to complete plate fracture. The resulting measured flexural-strength values are typically found to be only around 1 per cent of the theoretical material strength of glass (ca. 15–30 GPa) [8]. In sharp contrast, tensile strengths as high as 5 GPa have been achieved in glass fibres fabricated under tightly controlled laboratory conditions. This finding has been attributed to the near pristine fibre-surface finish.

As mentioned above, brittle failure in glass (as well as in the majority of brittle ceramics) is the result of nucleation (on pre-existing flaws) and propagation of the cracks. These processes are accompanied by local and global stress attenuation/relaxation and structure failure/fragmentation [6, 7]. Finite-element analyses have been extensively used over the last couple decades to elucidate the underlying

mechanisms and quantify the impact resistance of protective transparent structures under high-velocity impact and penetration conditions. In these analyses, most of the effort was typically devoted to modelling the complicated post-damage initiation response of ceramic materials (i.e. the mechanical/structural response of these materials to impact loads in the presence of cracks). In general, all the existing brittle-fracture models reported in the literature, can be categorized as being either: (a) continuum based [9–12] or (b) being of a discrete nature [13]. Since a detailed overview of these two groups of brittle-fracture material models was provided in our previous work [4, 5], only a brief description of these is provided below. Within the continuum-based approaches, glass is treated as a linear elastic material whose stiffness coefficients can degrade as a result of a cracking-induced damage within the material. Damage, itself, is treated as a continuum quantity which is obtained by homogenizing crack-laden material into an elastically equivalent crack-free continuum material with degraded stiffness. While within the continuum-based models, cracks are considered implicitly via their effect on the material stiffness, within the discrete models for brittle-fracture cracks (as well their nucleation, propagation, and coalescence processes) are treated explicitly. In other words, instead of smearing-out/homogenizing cracks into a crack-free material, cracks are recognized as discrete entities which locally disrupt the continuity in displacement/stress fields and lead to local stress-concentration effects.

Numerous experimental investigations carried out over the last 30 years [14–17] have clearly established that distinct differences exist in the mechanical behaviour of the tin-side and air-side surface of plate glass fabricated using a conventional float-glass process. These differences are predominantly manifested in the flaw-size populations, indentation/microhardness, and tensile/flexural strengths between the two plate-glass surfaces. Furthermore, it is well established that these differences are a consequence of different chemo-thermo-mechanical histories of the two surfaces resulting from the float-glass fabrication processes. These different processing histories are believed to either change the surface flaw population and/or chemically alter the surface layer of glass (mainly through ion-exchange with the tin bath). To better understand the origin of these differences, a brief overview of the conventional float-glass manufacturing process is provided in section 2.1.

While common transparent armour structures are made of cost-effective soda-lime glass, the subject material of the present investigation is borosilicate glass. When this material is fabricated in the form of

plate glass using the conventional float-glass process, it is commonly referred to as Borofloat. The predominant reason for focusing on borofloat is that this material has approximately 10 per cent lower mass-density than the comparable soda-lime-based glass (e.g. Starphire®).

The organization of this article is as follows: in sections 2.1 and 2.2, brief overviews are, respectively, provided of the float-glass fabrication process and of the past experimental efforts aimed at highlighting and clarifying the differences in the mechanical properties of the tin- and air-side surfaces and their subsequent effects on the overall impact resistance of glass-based protective transparent structures. In sections 3.1 and 3.2, brief summaries are, respectively, presented of our recent continuum-level physically based material model for soda-lime glass [4, 5] and of the proposed modifications/upgrades to this model to include the effects of tin- versus air-side microstructural/compositional differences and to reflect the borosilicate nature of the subject material. Details regarding the experimental and computational procedures used to generate the data needed for validation of the upgraded borofloat material model are discussed in sections 4.1 and 4.2, respectively. The main results obtained in this study are presented and discussed in section 5. The key conclusions resulting from this study are summarized in section 6.

2 FLOAT-GLASS FABRICATION AND MECHANICAL TESTING

2.1 Float glass fabrication

2.1.1 Fabrication process

Float glass is made using the Pilkington [18] process utilizing silica sand, boric acid, soda ash, limestone, with additional batch materials and other refining agents. These batch/constituent materials are mixed and subsequently combined with cullet (crushed glass) as they are fed into the melting zone of a multi-zone glass fabrication furnace. Within the melting zone of the furnace, preheated air and jets of natural gas are combined and combusted to create a torch-like flame producing temperatures of about 1300–1500 °C, melting the pre-mixed materials in minutes. Upon complete melting, the molten glass enters the next furnace zone to begin the so-called *fining process* during which the gas bubbles within the molten glass (common byproducts of the glass-melting process) are allowed to escape into the furnace atmosphere. After several hours of fining, the glass then flows into the *forming chamber* onto a molten tin bath at approximately 1100 °C. To ensure

uniform spreading of the molten glass onto the molten-tin bath (which can have lateral dimensions as large as 3–4 m) refractory guides are used to control the flow trajectory, while a canal gate is used to control the flow rate. Tin is chosen as the molten-glass float medium due to its relatively high density (which ensures that the glass remains buoyant), a low melting temperature (in order to lower manufacturing power consumption), immiscibility with molten glass (to minimize chemical contamination of the glass), and high cohesion (to minimize wetting of and adhesion to the tin-side as it solidifies). As the molten glass flows down the length of the forming chamber, it begins to cool creating a continuous ribbon of semi-solid material. To prevent the oxidation of tin and the formation of tin oxide (dross) which tends to adhere to glass, the forming chamber atmosphere is typically made up of nitrogen and hydrogen. Heating elements above the glass (which allow for strict temperature control of the glass face exposed to the forming chamber atmosphere, the glass air-side) and motor-driven stretching sprockets (which dig in to the molten glass at the ribbon edges) allow for precise control of the ribbon thickness.

As the glass exits the forming chamber, it has achieved its final thickness. Next, the glass ribbon enters the so-called *lehr chamber*, where it is cooled from an entrance temperature of 600 °C down to 200 °C at its exit. The rate of cooling is closely controlled in order to obtain the desired residual stress distribution through the ribbon thickness. Final cooling to room temperature is carried out on the open-air roller-type conveyer using an array of fans. During this time, the quality of the fabricated float-glass ribbon is inspected by a number of instruments to determine uniformity of thickness and the potential presence of surface flaws/imperfections. Once fully hard, the continuous glass ribbon is sectioned into discrete plates of predetermined dimensions. The sectioning process is typically carried out by scoring the ribbon surface with computerized numerically controlled carbide rollers and snapping the scored ribbon. The glass plates then continue along the main-line conveyers (while still having their tin-side in contact with the rollers) to a production-line inspection station where they are visually examined for surface or edge defects/imperfections. Before the glass plates are stacked for packing and shipping, they are dusted with a fine powder that acts as a separation medium.

2.1.2 Microstructure and flaw content of as-fabricated float glass

Under most applications of plate glass, the flaw content (particularly the one on the plate-glass

surfaces) is not high enough to significantly affect the functional performance of the glass structure. However, under extreme loading conditions, such as those encountered in the case of blast or high-velocity projectile impact, fabrication/handling-induced flaws can profoundly affect the impact resistance of plate glass. Based on the description of the float-glass process given above and various microstructural investigations of glass [14–17], it is clearly established that there are at least three main sources of flaws on the tin-side of plate glass.

1. Flaws induced through mechanical contact with conveyer rollers during the advancement of the glass ribbon and discrete glass plates along the production line. Conveyer roller damage is readily apparent (visible) when the glass ribbon exits the lehr and begins the final cooling stage as it is still soft and the rollers leave visible imprints at the ribbon edges. These ribbon edges are later removed through the use of a longitudinal scoring/breaking process similar to the one described above.
2. Flaws associated with tin-oxide particulates adhering to the tin-side surface. These tin-oxide particulates are made visible through the use of an ultraviolet radiation lamp which selectively illuminates the tin-oxide structure. In fact, this is the common procedure for identifying the tin-side in as-fabricated plate glass.
3. Flaws induced by tensile stresses associated with thermal gradients present within regions adjacent to the glass-ribbon/tin-bath interface.

In addition to the aforementioned changes in the flaw population on the plate-glass tin-side, it has also been demonstrated that tin can diffuse into glass via an ion-exchange process with silicon. A typical diffusion distance can be as large as 50 μm [19]. Within the glass, tin tends to integrate into silicate network as either SnO or SnO₂. As a result, the number of non-bridging oxygen atoms in glass is reduced leading to a decrease in the thermal expansion coefficient and an increase in the elastic modulus of the tin-enriched plate-glass surface layer. It is generally expected that these microstructural/compositional changes present at the plate-glass tin-side may also affect impact strength of the glass-based protective transparent structures.

As far as the air-side of the plate glass is concerned, its flaw population is going to be mainly dominated by the attendant thermal gradients experienced by the glass ribbon during the float-glass manufacturing process.

2.2 Mechanical tests used to reveal tin- versus air-side differences

An open-literature review carried out as part of this study revealed that a great amount of research effort has been put forth in the recent decades in order to experimentally characterize the mechanical response of float glass under various loading conditions and to highlight/quantify microstructure/property differences between the air-side and tin-side. The review also revealed that the most commonly utilized tests are the bi-axial flexure test (used to reveal the characteristic strength of the plate-glass back face that is subjected to tension) and indentation tests (based on the use of different indenter geometries, e.g. spherical and diamond tip, used to determine the critical indentation loads at the onset of various damage modes, e.g. Hertzian ring, radial, cone, or median cracks and material surface build-up surrounding the indentation). In addition, the following tests have also been employed.

1. *Klosky bar-type test*: a high-rate flexural test used to reveal strain-rate dependency of the material mechanical response.
2. *Dilatometry* – used to determine the coefficient of thermal expansion.
3. *Sonic resonance* – used to determine the material local, elastic modulus.
4. *Dynamic fatigue tests* – used to quantify the effect of moisture on the strain-rate dependency of glass strength.
5. *Fractography* – used to determine the pre-existing surface-flaw geometry and dimensions.

The literature review carried out in this study revealed the following main experimental findings regarding the (microstructural/property) differences and similarities between the air-side and the tin-side.

1. The air-side characteristic flexural strength (one of the failure probability Weibull-distribution parameters) is typically greater by a factor between 1.2 and 2.0 relative to that of the tin-side [15–17].
2. The average air-side flaw size is generally smaller by a factor of 1.5–2.0 relative to its tin-side counterpart [16, 17]. This finding is clearly consistent with that made in (1) and can be attributed to damage induced by mechanical contact of the glass ribbon tin-side with the conveyer rollers.
3. Both the air- and tin-sides of borofloat plate glass show a positive stress-rate dependence of their characteristic strength and the two dependences are quite comparable [17].
4. The air-side Weibull modulus (the second Weibull-distribution parameter) is in general smaller by a

factor of 1/3–1/2 relative to the tin-side [16]. This finding and the one stated in (1) indicate that the air-side flaw distribution is broader (associated with a smaller value of the Weibull modulus) and shifted towards higher strength levels in the air-side case. Also, this finding suggests that mechanical contact between the tin-side and the conveyer rollers results not only in more potent (larger) flaws, but also in a narrower distribution of flaw-size, while on the air-side flaw generation is a more random process which yields a broader flaw-size distribution.

5. The tin-side elastic modulus is typically ca. 15 per cent higher than its air-side counterpart [19]. As stated earlier, this finding can be attributed to the fact that, at the tin-side, SnO and SnO₂ are incorporated into the silicate network resulting in a reduced fraction of non-bridging oxygen atoms and result in an increase in the overall network connectivity.
6. The tin-side coefficient of thermal expansion is typically lower by about 20 per cent compared with its air-side counterpart [19]. This finding can be explained using the same argument as that presented in (5).
7. The tin-side indenter critical load associated with the nucleation of Hertzian ring cracks (the first type of cracks to form during a spherical-indenter indentation test) is on average 15 per cent higher than its air-side counterpart [15]. This finding appears to be related to one given in (5) which indicated a higher compliance of the air-side surface layer.

3 GLASS MATERIAL MODEL – OVERVIEW AND EXTENSION

3.1 A brief overview of the soda-lime glass material model

3.1.1 Physical foundation of the model

The soda-lime glass material model developed in our previous work [4, 5] was an attempt to account for the fact that the mechanical response of soda-lime glass is drastically different under low-deformation rate (i.e. quasi-static) and high-deformation rate (i.e. impact) loading conditions [1, 2]. Under quasi-static loading conditions, glass typically fails by the propagation of a single or a couple of discrete cracks and only a few fragments are created after complete fracture. In sharp contrast, under dynamic loading conditions, glass tends to undergo substantial damage (resulting from the formation of a large number of micron and submicron-size cracks) and tends to

undergo comminution (i.e. forms a large number of sub-millimetre size fragments). In both cases, however, the failure is believed to be controlled by pre-existing flaws which, when subjected to sufficiently large (tensile or shear) stresses, can become cracks. A brief overview of the two failure regimes (i.e. the quasi-static coarse-fragmentation regime and the dynamic comminution regime) is presented below while a more quantitative discussion of the same can be found in references [4, 5].

The occurrence of the two fracture regimes is believed to be the result of the competition between two internal processes accompanying loading of glass.

1. Crack formation at the pre-existing flaws and crack growth. The nucleation of cracks is accompanied by the formation of so-called 'shielding' zones, i.e. the zones surrounding the cracks within which the stresses are highly relaxed and the probability for nucleation of additional cracks is very small.
2. The increase in stress level due to continued loading which promotes the formation of additional cracks (at less potent pre-existing flaws).

Since the crack formation process is typically associated with mechanical instability (i.e. once a crack is nucleated it continues to grow at a terminal velocity until it reaches the free surface or another crack), low loading rates tend to promote the coarse fragmentation fracture regime. In other words, once a crack or a couple of cracks are formed, they can extend over the entire structure before the stress at other flaws has reached a high enough level to form additional cracks. Conversely, high loading rates promote the formation of a large number of cracks, i.e. the critical stress level for crack nucleation is reached at many pre-existing flaws before the previously nucleated cracks have a chance to extend far enough and shield these flaws from the externally applied stress.

3.1.2 Simplifying assumptions and basic components of the model

The following are the key simplifying assumptions and basic components of the model developed in references [4, 5].

1. The distribution of pre-existing flaws throughout the material was assumed to follow the Weibull-type distribution with different distribution parameters being used for the surface/near-surface regions and the bulk region of glass target plate.
2. Both the nucleation of microcracks (which leads to comminution) and that of macrocracks (which

leads to coarse fragmentation) were postulated to be governed by the same maximum principal normal stress-based damage (mode I cracking) initiation criterion.

3. It was further assumed that it is the loading/stress rate at the moment of crack nucleation which determines if a crack will remain a single macrocrack within the given finite element resulting in the coarse-fragmentation failure mode of the element or the crack will be accompanied by the formation of many additional microcracks leading to progressive damage and ultimate fine-fragmentation failure of the element. To separate these two regimes of fracture within the bulk and the surface regions, competition between the coarse- and fine-fragmentation modes was analysed under constant stress-rate loading conditions. This procedure yielded separate values for the critical stress-rate associated with this transition for the bulk and surface regions, respectively. At stress rates below the critical value, a single crack fracture regime was assumed while at stress rates above it a multiple-crack regime was adopted.
4. When a material element begins to fail via the single-crack mode, the (single) crack nucleated within that element (in accordance with the aforementioned stress-based damage-initiation criterion) was assumed to extend at the terminal velocity. Further growth of the crack is governed by a fracture toughness-based crack growth criterion. This is accomplished as follows: (a) adjacent failed elements aligned in a particular direction are used to define the associated crack length in that direction; (b) for an element located at a crack tip, the mode-I stress intensity factor K_I is calculated by multiplying its maximum principal stress with a factor $\sqrt{\pi a}$, where a is the crack half-length; and (c) then, crack extension occurs by failure of an element described in (b) when the following condition is satisfied: $K_I > K_{IC}$, where K_{IC} is the material mode-I critical stress intensity factor.
5. When an element is undergoing fracture via the growth of the single-crack, stiffness and strength properties of this element were assumed to linearly degrade with the corresponding crack strain from the point of crack initiation to the point of complete traversal of the element by the crack.
6. Once an element has started undergoing (coherent) damage due to the formation of multiple cracks, stress-shielding and path-crossing effects prevent, initially, the nucleation of macrocracks. However, when the extent of coherent damage within a single element reaches a (stress-rate

invariant) critical value, this element was assumed to fracture by microcrack coalescence and to lose most of its ability to support load. To account for the experimental observations that the resulting microfragments are typically confined by the surrounding non-fractured material and can support compressive and shear loads, failed elements are assigned small residual levels of shear modulus and strength.

- When an element is subjected to coherent damage, the extent of damage was taken to be governed by a damage evolution equation and the extents of degradation of the corresponding stiffness and strength properties of the material were assumed to be governed by the appropriate damage-dependent stiffness and strength material constitutive relations.

3.2 Modification and enhancement of the model

The soda-lime glass material model developed in our prior work [4, 5] was, for the most part, retained in its original formulation, and only the modifications/enhancements listed below were made. Since detailed accounts of the mathematical formulation of the soda-lime glass model and the procedure employed for its parameterization can be found in references [4, 5], these details will not be presented here.

- In order to apply the original model to borofloat various structural (e.g. density), mechanical (e.g. stiffness, critical stress intensity factor, critical level of coherent damage at which crack coalescence takes place, etc.), and flaw-size distribution (e.g. the characteristic strength and the Weibull modulus) parameters were re-evaluated using various open-literature sources [15, 16]. A summary of the material-model parameters is provided in Table 1. The reader is referred to references [4, 5] for the explanation of the symbols appearing in Table 1.
- To take into account the aforementioned effect of flaw-size distribution differences between the air-side and the tin-side, different values of two-parameter Weibull-distribution parameters are assigned to the corresponding plate-glass surface-material layers; a total of three (one bulk and two surface) failure probability distributions are now considered. A list of the associated Weibull-distribution parameters is provided in Table 1.
- Using the procedure outlined in references [4, 5], the critical stress rate at which a transition in the fracture mode between the quasi-static coarse-

Table 1 Material-model parameters for borosilicate glass used in this study

Property	Symbol	Value	Unit
Density	ρ	2230	kg/m ³
Mean fracture toughness	K_{IC}	0.75	MPa m ^{1/2}
<i>Air-side surface</i>			
Young's modulus	E	63.0	GPa
Poisson's ratio	ν	0.18	–
Weibull modulus	m	6.7	–
Mean static fracture strength	$\sigma_{f,static}$	130.6	MPa
Effective surface	Z_{eff}	1599	mm ²
<i>Tin-side surface</i>			
Young's modulus	E	69.3	GPa
Poisson's ratio	ν	0.18	–
Weibull modulus	m	4.0	–
Mean static fracture strength	$\sigma_{f,static}$	111.9e6	MPa
Effective surface	Z_{eff}	1599	mm ²
<i>Bulk material</i>			
Young's modulus	E	63.0	GPa
Poisson's ratio	ν	0.18	–
Weibull modulus	m	30.0	–
Mean static fracture strength	$\sigma_{f,static}$	250.0	MPa
Effective volume	Z_{eff}	1.0e5	mm ³

fragmentation regime and the dynamic comminution regime takes place was evaluated as: (a) 3.9 MPa/ μ s for the bulk material, (b) 7.9 MPa/ μ s for the air-side surface material, and (c) 9.5 MPa/ μ s for the tin-side surface material.

- While, in the previous rendition of the model [4, 5], the formation of isolated cracks was allowed to take place only within the bulk portion of the plate glass, in the present model such cracks are allowed to also nucleate at the plate-glass surfaces. The reason that formation of surface macrocracks was neglected in our previous work was that the material model was primarily used in edge-on impact analyses of glass plates in which these cracks are found to be predominantly located within the bulk [1, 2]. In this study, on the other hand, macrocracks were allowed to nucleate at plate-glass surfaces in order to comply with numerous experimental investigations which revealed that, during frontal impact, cracks can nucleate both at the strike face (e.g. concentric ring cracks, radial cracks, etc.) as well as at the back face (e.g. radial cracks).
- In our previous model, discrete cracking of an element was assumed to result in an isotropic damage, i.e. a *cracked* element was assumed to remain isotropic (although with a substantially degraded elastic modulus). In this study, this simplification as not implemented and instead discrete cracking is assumed to produce an orthotropic degraded material. In other words, the associated damage was no longer represented using a single scalar damage variable, but rather a second order damage tensor.

4 EXPERIMENTAL AND COMPUTATIONAL PROCEDURES

4.1 Experimental procedure

The experimental procedure used in this study employed the impact of a stainless steel projectile onto a transparent target laminate consisting of a borofloat plate adhesively bonded to a polycarbonate backing plate of equal lateral dimensions. The experiment was originally intended to be carried out using only 5.53 mm (0.218 in) diameter ball bearing (BB) projectiles (designation: SS 440C), but they proved unable to penetrate the transparent target laminate and therefore these projectiles were complemented with more massive 5.51-mm diameter, 5.51-mm height right circular cylinders (RCC, designation: SS 440C) and with steel fragment-simulating projectiles (FSP) in the shape of a RCC with a flat-nosed chisel tip with dimensions of 5.46 mm diameter and 6.40 mm height. Each laminated test panel had a square shape with a nominal edge length of 101.6 mm (4 in). The thickness of the glass plate strike face was either 3.175 mm (1/8 in) or 6.35 mm (1/4 in), and in each case the glass plate was bonded using a 2.5-mm (1/10 in) polyurethane (PU) adhesive interlayer to a 3.175-mm (1/8 in) polycarbonate backing plate. A total of 32 transparent laminates were tested, where an equal number of test laminates had their outward-facing surface as the borofloat plate tin-side and air-side. The test matrix is displayed in Table 2.

The experimental test setup consisted of the following main components:

- a gas gun capable of charge pressures up to 10.69 MPa (1550 lbf/in²) with a 22-caliber rifled barrel (Fig. 1);
- a ring-shaped lamp housing eight halogen bulbs;
- a square-frame mounting fixture (used for securing the 101.6 mm (4 in) square test target) which is bolted at each of the four corners to the test-setup safety enclosure;
- the (aforementioned) polycarbonate safety enclosure that houses the back-light ring lamp and the mounting fixture;
- two high-frame rate video cameras (Photron FASTCAM SA1.1 model 675K-M1) with a

Table 2 Experimental test matrix indicating the number of single-shot tests for different configurations of three-lamina transparent armour structures employed in this study

	Air-side impact	Tin-side impact
3.175 mm borosilicate glass		
2.54 mm polyurethane	15*	9 [†]
3.175 mm polycarbonate		
6.35 mm borosilicate glass		
2.54 mm polyurethane	2 [‡]	2 [§]
3.175 mm polycarbonate		

*In five tests BB, and in ten tests RCC projectiles were used.

[†]In two tests BB, and in seven tests RCC projectiles were used.

[‡]In one test, an RCC and in one test an FSP was used.

[§]In two tests, RCC projectiles were used.

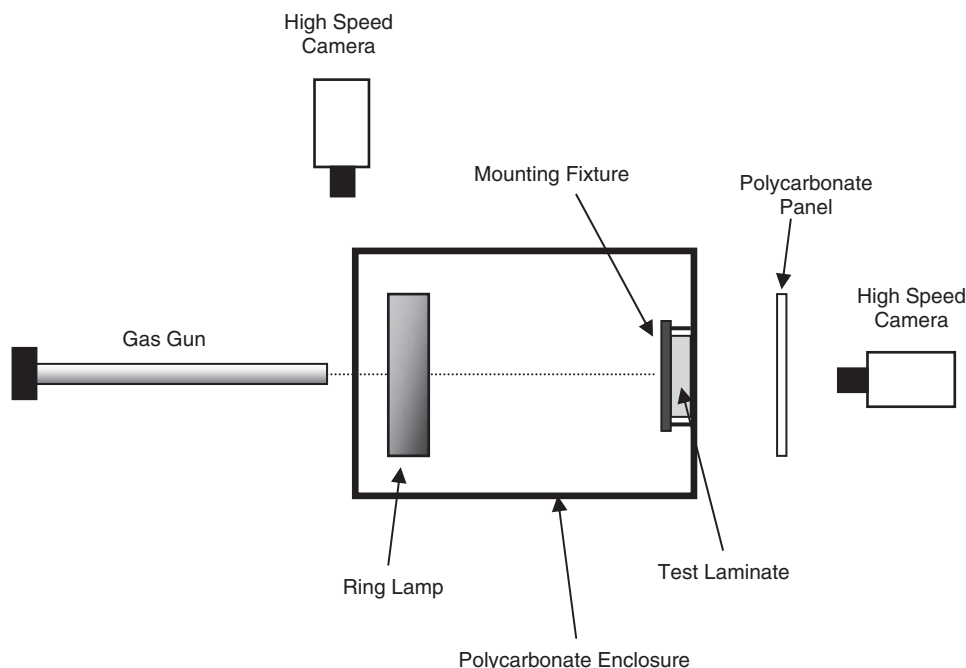


Fig. 1 Gas gun-based experimental setup for impact resistance testing

maximum frame rate of 675 000 frames/s (a frame rate of 300 000 frames/s was used in the present analysis).

The employed test procedure typically involves the following steps.

1. The transparent test laminate is secured within the safety enclosure using the mounting fixture.
2. While ensuring that the ring-lamp is powered on, a thin-paper light filter with a small hole for the projectile is placed on the strike face of the target in order to help diffuse the light from the ring lamp.
3. The gas gun barrel is loaded with a projectile by first removing the barrel plug/holding clamp, hand-placing the projectile into the barrel, and then replacing the barrel-loading plug and its clamp.
4. The desired gas gun charge pressure is achieved by exposing, via a manual twist valve, the gas gun pressure vessel to a large-capacity high-pressure carbon dioxide cylinder, while monitoring the gas gun pressure gauge and then shutting the valve at the desired pressure level.
5. The gas gun is then remotely fired by an electronic switch that activates the solenoid valve which allows the pressurized gas to instantaneously enter the gun barrel.
6. The projectile is accelerated down the barrel length by the expanding gas and exits the barrel (at a velocity of a few hundred metres per second) into the polycarbonate safety enclosure.
7. The projectile continues along its trajectory through the centre of the ring lamp and impacts the target.

Within the test procedure described above, the following measurements are typically carried out.

1. A high-speed camera aligned perpendicular to the projectile trajectory is used to track/capture the advancement of the projectile after leaving the gun barrel. The frame capture from this camera is subsequently imported into an image processing software to determine the projectile velocity.
2. The second camera, aligned directly along the projectile trajectory and located behind the target, is used to capture the temporal evolution of the target/projectile material deformation, damage, and fracture. The frame capture from the second camera is also imported into the image processing software to determine the propagation velocity of discrete macrocracks as well as the propagation velocity of the dark-region/coherent damage front within the glass plate.

The experimental procedure described above was also used to determine the so-called *V50*, i.e. the velocity at which the projectile has a 50 per cent

chance of fully penetrating the test laminate. Towards that end, the so-called *walk-up* procedure was employed. Within this procedure, the projectile velocity was incrementally increased until further increases in the projectiles' velocity continue to result in laminate full penetration. Then, *V50* is defined as an arithmetic mean of the lowest velocity at which full penetration is observed and the highest velocity at which penetration is incomplete.

4.2 Computational procedure

In this section, a brief description is provided regarding the construction of the geometrical and mesh models for the laminated glass/polycarbonate-based test panels and the stainless steel projectiles, as well as the computational procedure used to simulate the projectile initial frontal impact and subsequent penetration of the laminated test panels as experimentally carried out as part of this study.

4.2.1 Geometrical model

The first step in the present computational investigation included the development of geometrical models for the transparent laminated test panels and the projectiles with geometrical dimensions, constituent materials, and lamination sequences identical to their experimental counterparts described in the previous section. Since only the case of a normal impact was considered in this study, advantage is taken of the inherent symmetry of the geometrical model, i.e. only one quarter of the model is analysed.

4.2.2 Meshed model

Typically, the transparent laminated test panels were meshed using 105 000 first-order eight-node reduced-integration cuboidal elements with a nominal edge length dimension of 0.6 mm. On the other hand, projectiles were in general meshed using 230 first-order eight-node reduced-integration cuboidal elements with an average edge length of 0.55 mm. An example of the typical meshed model used in this study is displayed in Fig. 2. The mesh size was initially varied in order to validate that the results are not significantly mesh-size dependent. To prevent hour-glassing effects which may arise due to the use of reduced-integration elements, a default value of hour-glass stiffness was used.

4.2.3 Materials

To construct the transparent laminated test panels, three materials (borofloat, polyurethane,

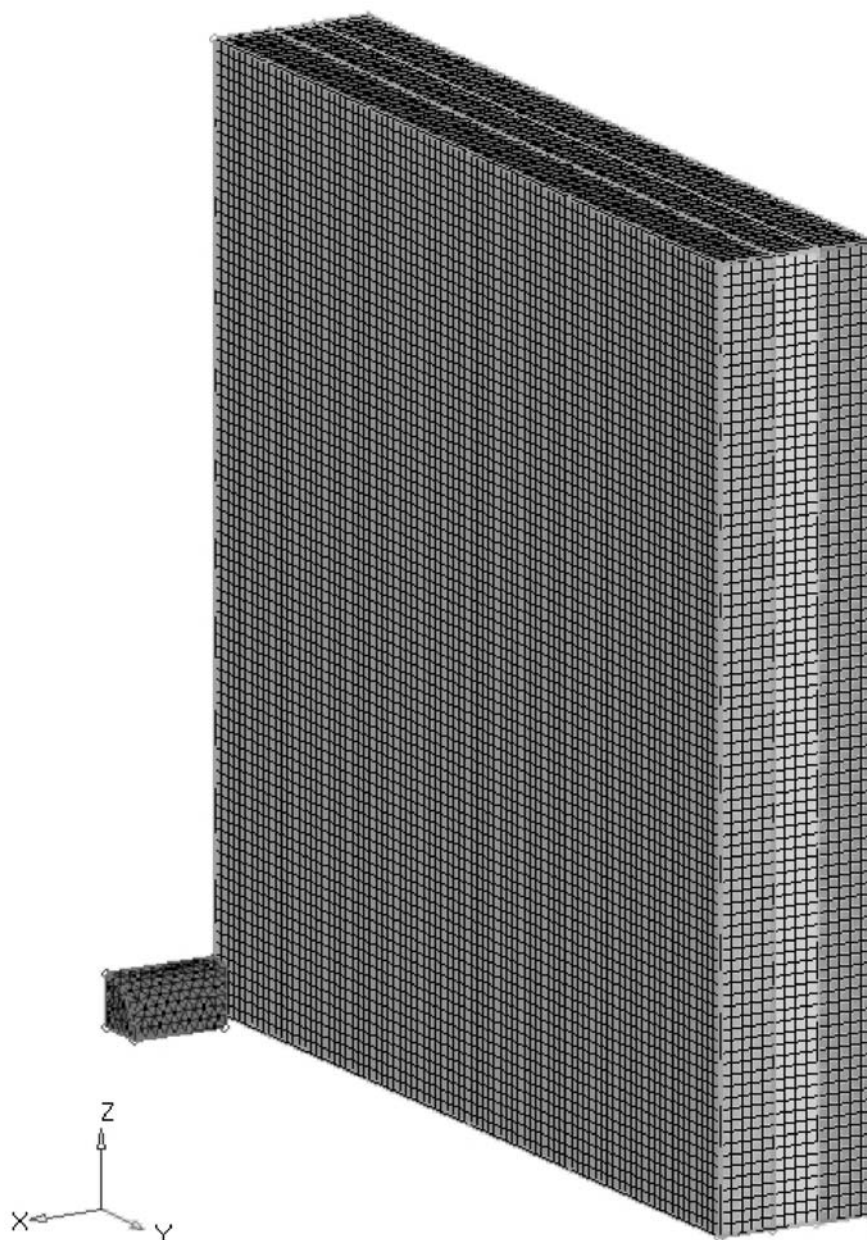


Fig. 2 An example of the finite element mesh used in the one-quarter model of the polyurethane-bonded glass/polycarbonate transparent test laminate

and polycarbonate) were used, while the various projectiles were constructed from their respective stainless steel grades. Borofloat was modelled using the material model developed in this study, while the material models for polyurethane, polycarbonate, and the stainless steels used can be found in our previous work [20, 21].

4.2.4 Contact interactions

Interactions between the projectile and the target as well as between different fragments of the target are modelled using the *hard contact pair* type of

contact algorithm. Within this algorithm, contact pressures between two bodies are not transmitted unless the nodes on the *slave surface* contact the *master surface*. No penetration/over closure is allowed and there is no limit to the magnitude of the contact pressure that could be transmitted when the surfaces are in contact. Transmission of shear stresses across the contact interfaces is defined in terms of a static, μ_{st} , and a kinematic μ_{kin} , friction coefficient and an upper-bound shear stress limit, τ_{slip} (a maximum value of shear stress which can be transmitted before the contacting surfaces begin to slide).

4.2.5 Initial and boundary conditions

The impact of the projectile with the target is modelled by assigning an initial (translational) velocity to the projectile (*the initial condition*). The initial velocity of the target was set to zero and, during the impact simulation, the laminated test panel faces that were framed between the mounting fixture and the polycarbonate safety enclosure were kept at a fixed position (*the boundary conditions*).

4.2.6 Solver and material-model implementation

All the calculations were carried out using ABAQUS/Explicit computer program [22]. The new material model for borosilicate glass was implemented into a VUMAT User Material Subroutine and linked with ABAQUS/Explicit.

4.2.7 Computational cost

No mass-scaling algorithm was used to increase the maximum stable time increment. Computational analyses were run on a machine with dual 2.83 GHz quad-core Intel Xeon processors with 8 GB of RAM. It should be noted that due to the non-local nature of the glass material model used (that is, calculation of the stress intensity factor within a given element/integration point requires knowledge of the material status for the surrounding elements/material points), each calculation could be carried out only using a single computational core of the machine. On the other hand, multiple simulations could be run simultaneously. A typical 150 μs projectile/target computational analysis would require ca. 30 min (wall-clock time).

5 RESULTS AND DISCUSSION

5.1 Experimental results

5.1.1 Damage mode characterization

A selection of the typical high-speed photography results obtained in this study is displayed in Figs 3 to 10. In each of these figures, shadow graphs corresponding to the post-impact times of 0, 6.6, 13.3, 36.6, and 83.3 μs in addition to a post-mortem shadowgraph are presented. These times roughly correspond to the ones associated with the occurrence of the main damage evolution events (e.g. initiation of discrete/macrocracks at the edge of the small coherent damage zone occurs at ca. 6.6 μs). The odd-numbered figures are associated with air-side impacts, while the

even are their tin-side impact counterparts. Figures 3 and 4 are associated with the use of BB projectiles while the remaining six figures utilize the RCC projectile. Figures 3 to 8 are associated with the thinner 3.175-mm thick borofloat glass strike face, while Figs 9 and 10 are associated with the thicker 6.35-mm thick borofloat glass strike face. The results displayed in Figs 5 to 8 are associated with the same projectile type and glass lamina thickness, the projectile initial velocity was lower (493 m/s) in the former and higher (540–596 m/s) in the latter case.

Careful examination of the results displayed in Figs 3 to 10 revealed that basically the same damage modes and the same general sequence of damage evolution occurs in all eight impact cases. Hence, the results displayed in these figures could be jointly described as follows.

1. The 0 μs frame corresponds to the moment of projectile impact onto the glass laminate which is identified by the appearance of a relatively bright spot (when contrasted with the grey coloured, undamaged surrounding material) at the location of impact.
2. The 6.66 μs frame is characterized by the clear appearance of: (a) a circular, dark-coloured coherent-damage zone. This zone contains a high density of light-scattering microcracks and thus appears as a contiguous dark region. The radius of this region is roughly twice the radius of the projectile; and (b) numerous, discrete, equally spaced, linear radial macrocracks emanating from the edge of the coherent damage region. The formation of radial cracks is typically an indication of the development of large tensile hoop stresses. These stresses are most likely the result of glass lamina material radial motion accompanying the projectile penetration into the target. As the material is displaced radially outward, it undergoes circumferential stretching (since the circumference increases with the radial distance from the point of impact). For clarity, the coherent region and the discrete cracks (as well as the other pertinent damage entities discussed below) are labelled in Fig. 3.
3. The predominant event in the 13.3 μs frame is the formation of a ring crack which connects the cracks fronts of all the outward-propagating radial cracks. The formation of the ring crack can be understood in the following way: (a) a combination of the central circular damage region and the adjacent radial cracks results in the formation of an array of radially oriented cantilever beams; (b) the dynamic load transferred from the projectile to the glass lamina produces target flexion and accompanying large bending moments at the end

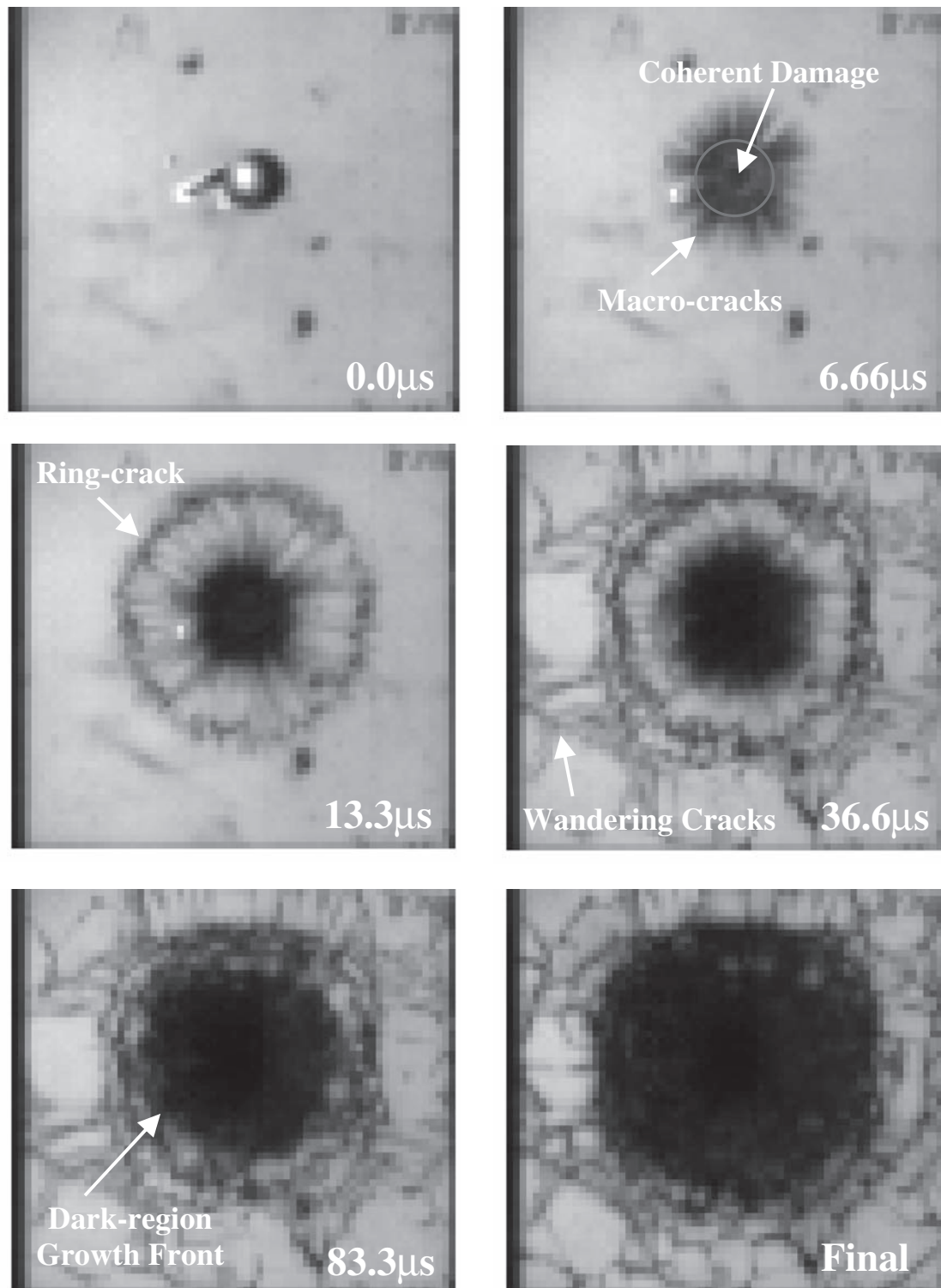


Fig. 3 Temporal evolution of damage in a 3.18-mm thick borofloat glass plate bonded to a 3.18-mm thick polycarbonate plate using a 2.54-mm thick polyurethane interlayer. Projectile: 5.53-mm diameter steel BB, velocity = 487 m/s, and strike face = air side

of the beams which coincide with the radial crack fronts; (c) when the associated radial tensile/bending stress becomes equal to the local material strength, failure occurs forming a segment of the ring crack. This process is circumferentially

repeated until the ring crack is completed. Meanwhile, relatively slow growth of the central coherent damage zone is observed.

4. The 36.6 μ s frame is characterized by appearance of numerous, discrete, randomly distributed,

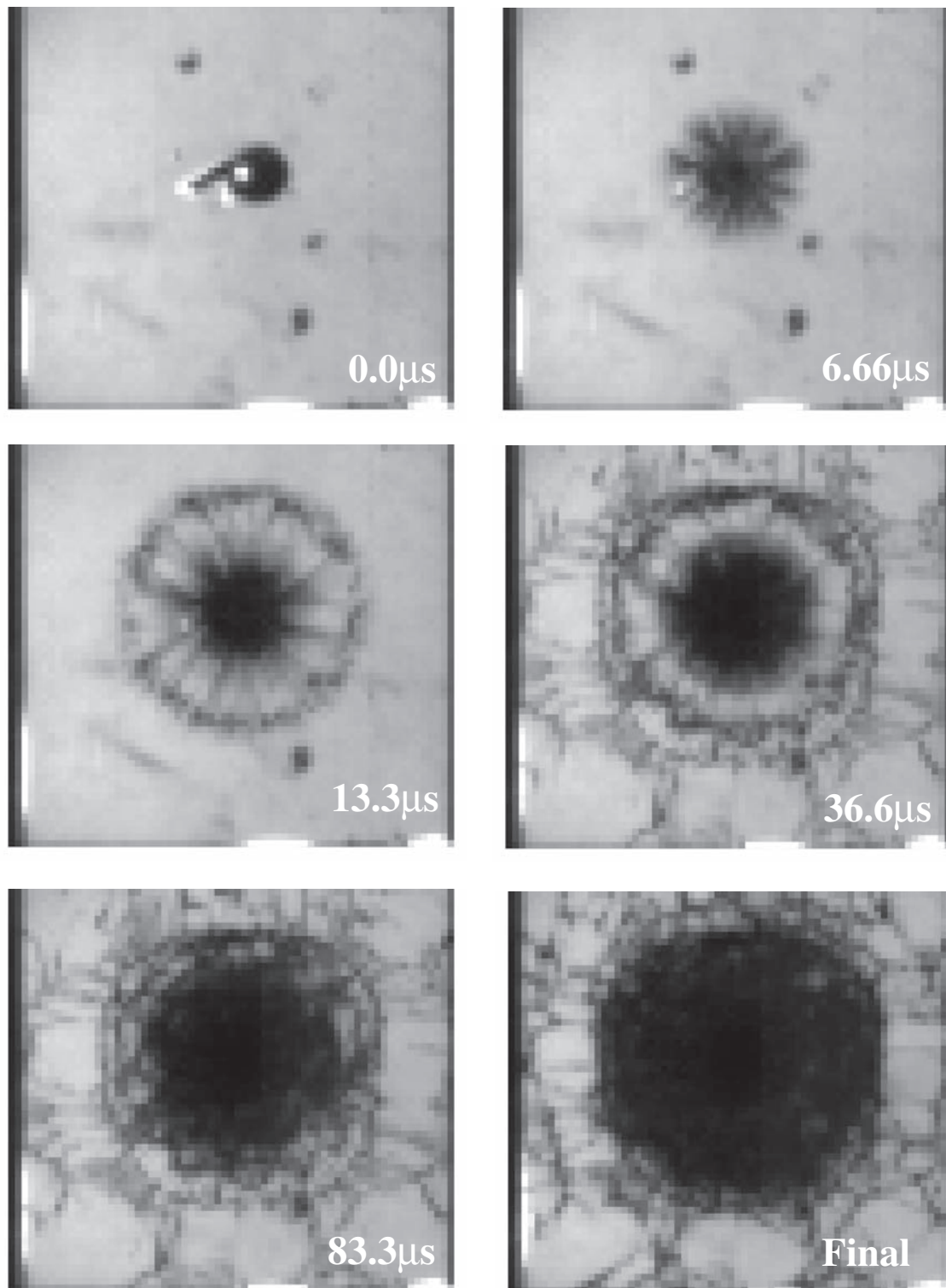


Fig. 4 Temporal evolution of damage in a 3.18-mm thick borofloat glass plate bonded to a 3.18-mm thick polycarbonate plate using a 2.54-mm thick polyurethane interlayer. Projectile: 5.53-mm diameter steel BB, velocity = 470 m/s, and strike face = tin side

wandering (with an overall outward radial trajectory) macrocracks emanating from the ring-crack outer face. The complex morphology and trajectory of these cracks appear to be related to a highly complex loading in this region resulting

from the reflection (at the framed edges and ring-crack outer face) and interaction of various compression and decompression stress waves. As in the 13.3 μs frame, relatively slow growth of the central contiguous damage zone is observed.

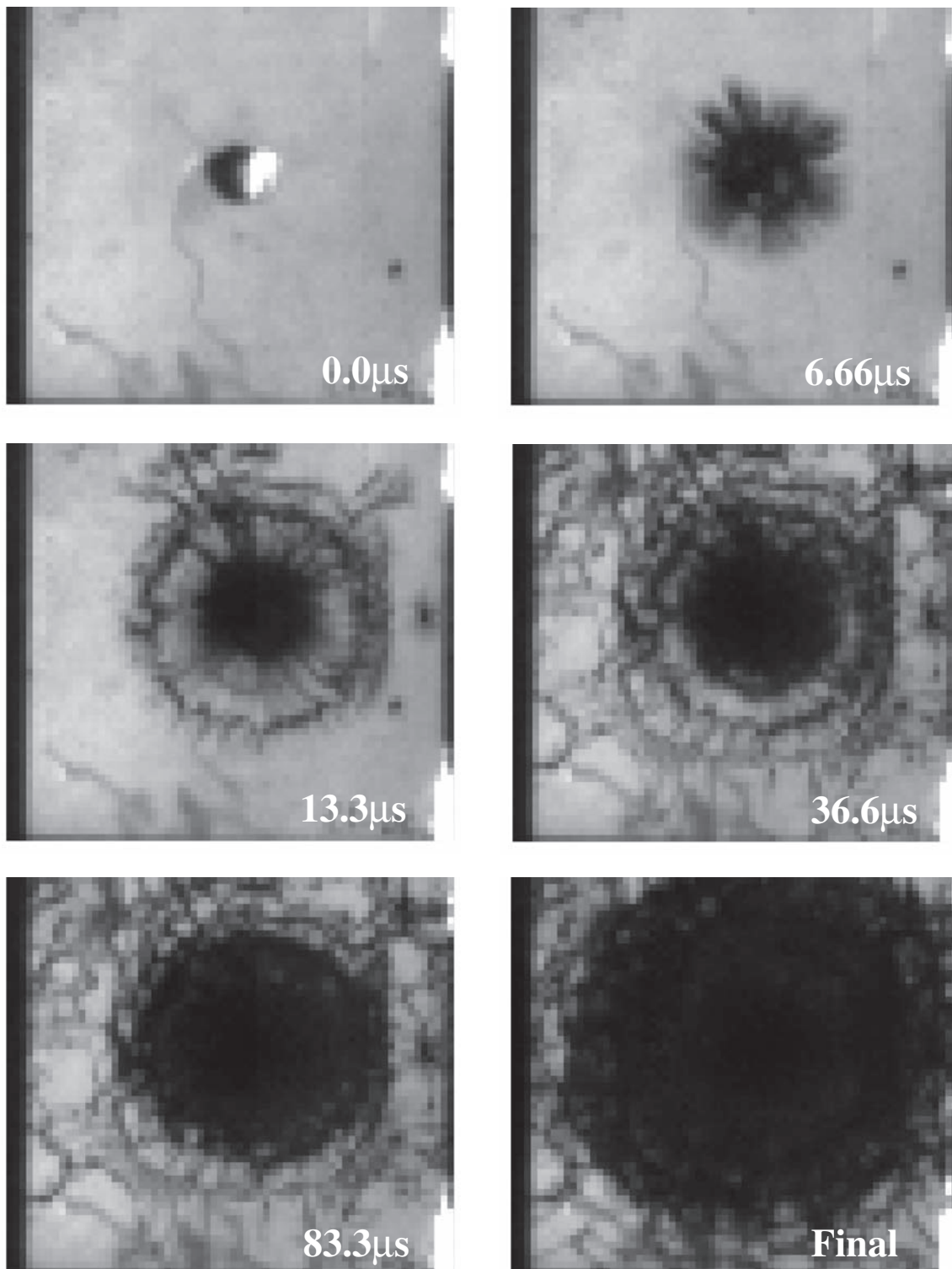


Fig. 5 Temporal evolution of damage in a 3.18-mm thick borofloat glass plate bonded to a 3.18-mm thick polycarbonate plate using a 2.54-mm thick polyurethane interlayer. Projectile: $5.51 \times 5.51 \text{ mm}^2$ steel RCC, velocity = 493 m/s, and strike face = air side

5. The 83.3 μs frame is characterized by two main observations: (a) low-rate random nucleation of discrete wandering macrocracks throughout the non-coherent damage region. This process is again

related to the associated complex transient stress state and (b) extension of the dark-coloured (contiguous) region front to the ring-crack interface. Post-mortem examination revealed that while

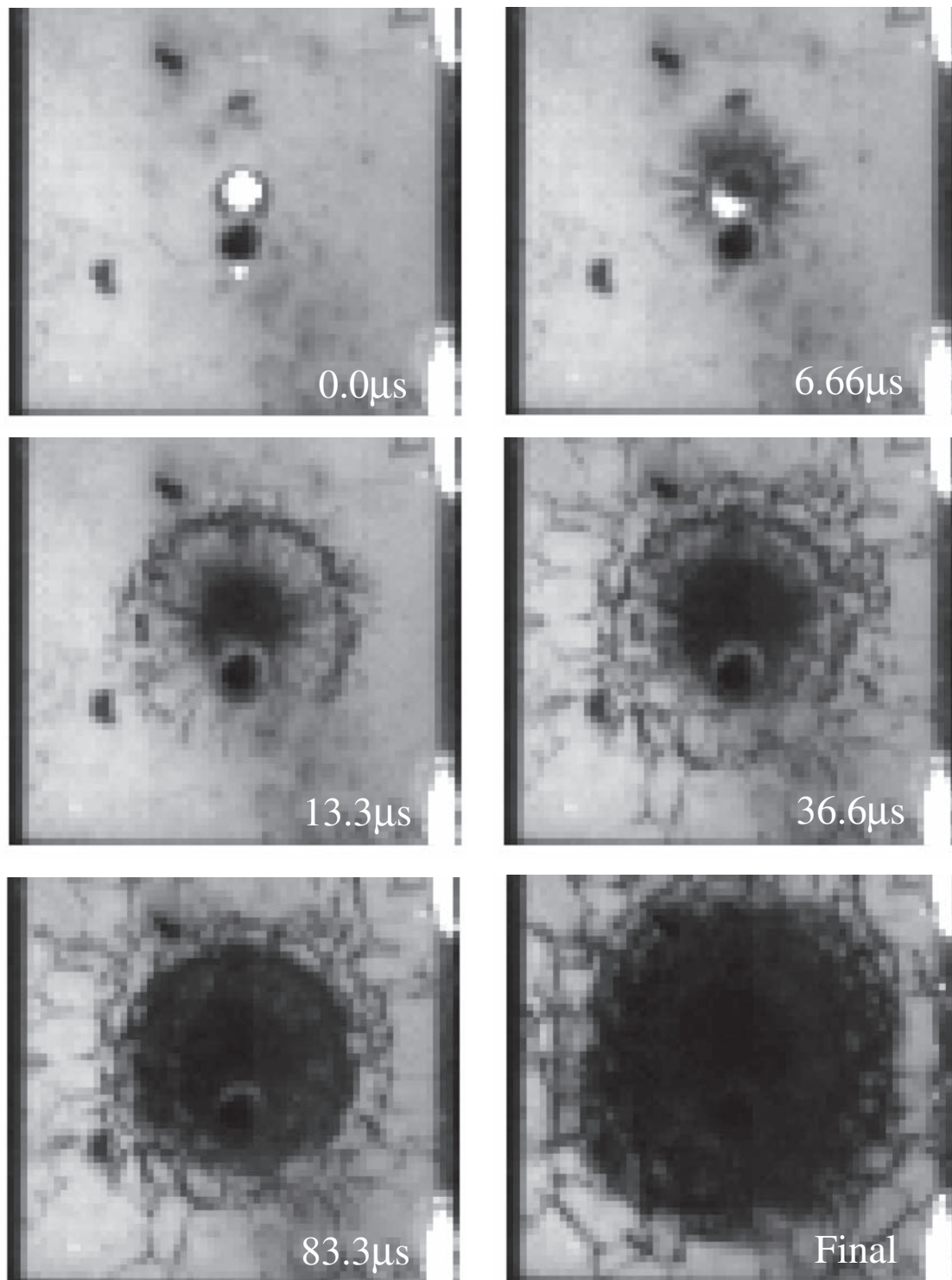


Fig. 6 Temporal evolution of damage in a 3.18-mm thick borofloat glass plate bonded to a 3.18-mm thick polycarbonate plate using a 2.54-mm thick polyurethane interlayer. Projectile: $5.51 \times 5.51 \text{ mm}^2$ steel RCC, velocity = 493 m/s, and strike face = tin side

initially this extension was predominately attributed to the evolution of coherent damage, at later post-impact times the growth of this region was dominated by the progression of decohesion and damage at the glass/polyurethane interface.

6. The final state of damage is fairly similar to that observed in the $83.3 \mu\text{s}$ frame except that the extents of macrocrack nucleation/growth and glass/polyurethane decohesion/damage are somewhat greater.

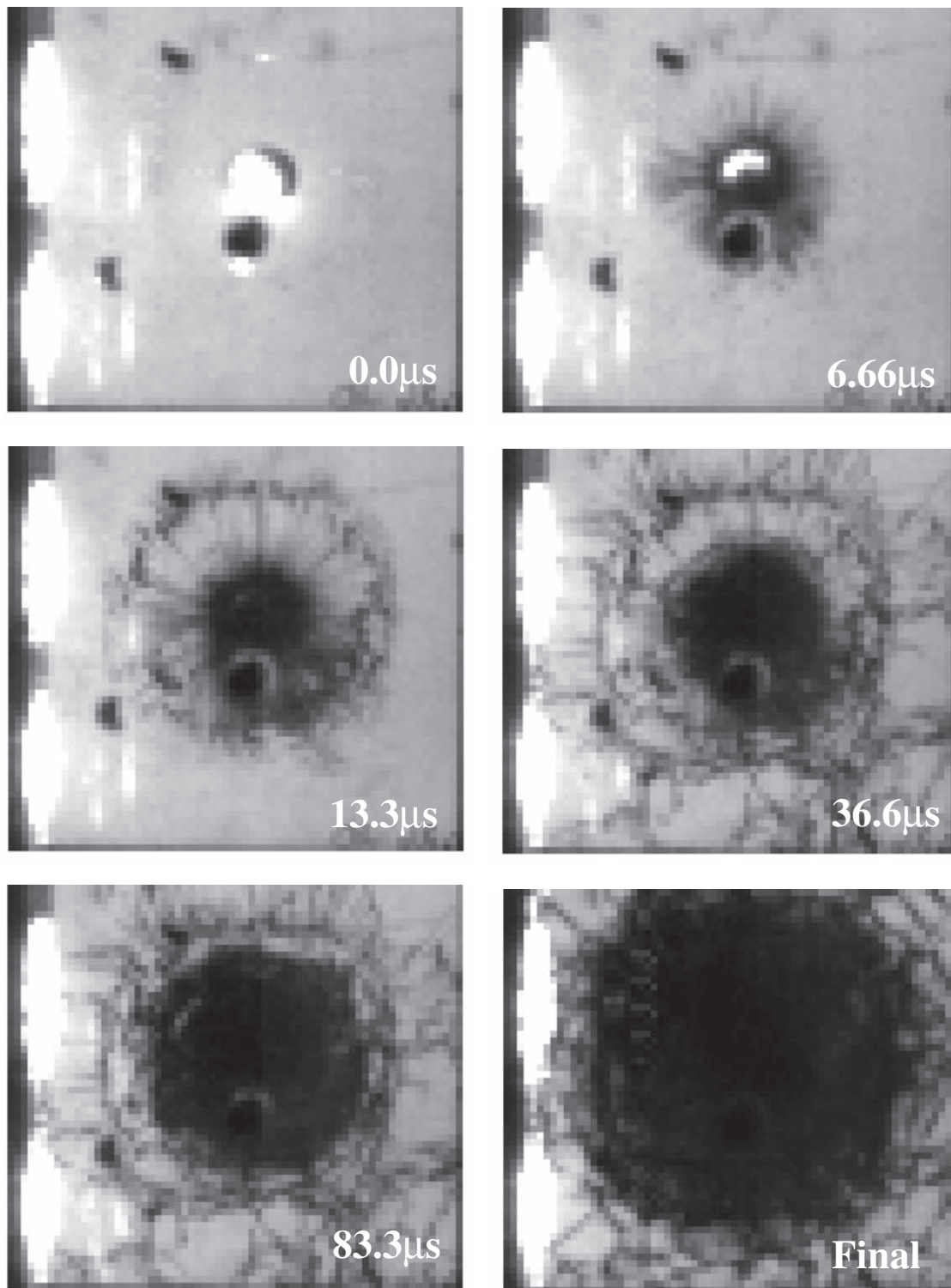


Fig. 7 Temporal evolution of damage in a 3.18-mm thick borofloat glass plate bonded to a 3.18-mm thick polycarbonate plate using a 2.54-mm thick polyurethane interlayer. Projectile: $5.51 \times 5.51 \text{ mm}^2$ steel RCC, velocity = 540 m/s, and strike face = air side

5.1.2 Evolution kinetics and spatial distribution of damage

To facilitate the analysis of the quantitative results, a summary of the experimental test

conditions is provided in Table 3. This is followed by Table 4 in which a summary is provided of the main post-impact quantities measured and the associated values obtained in this study.

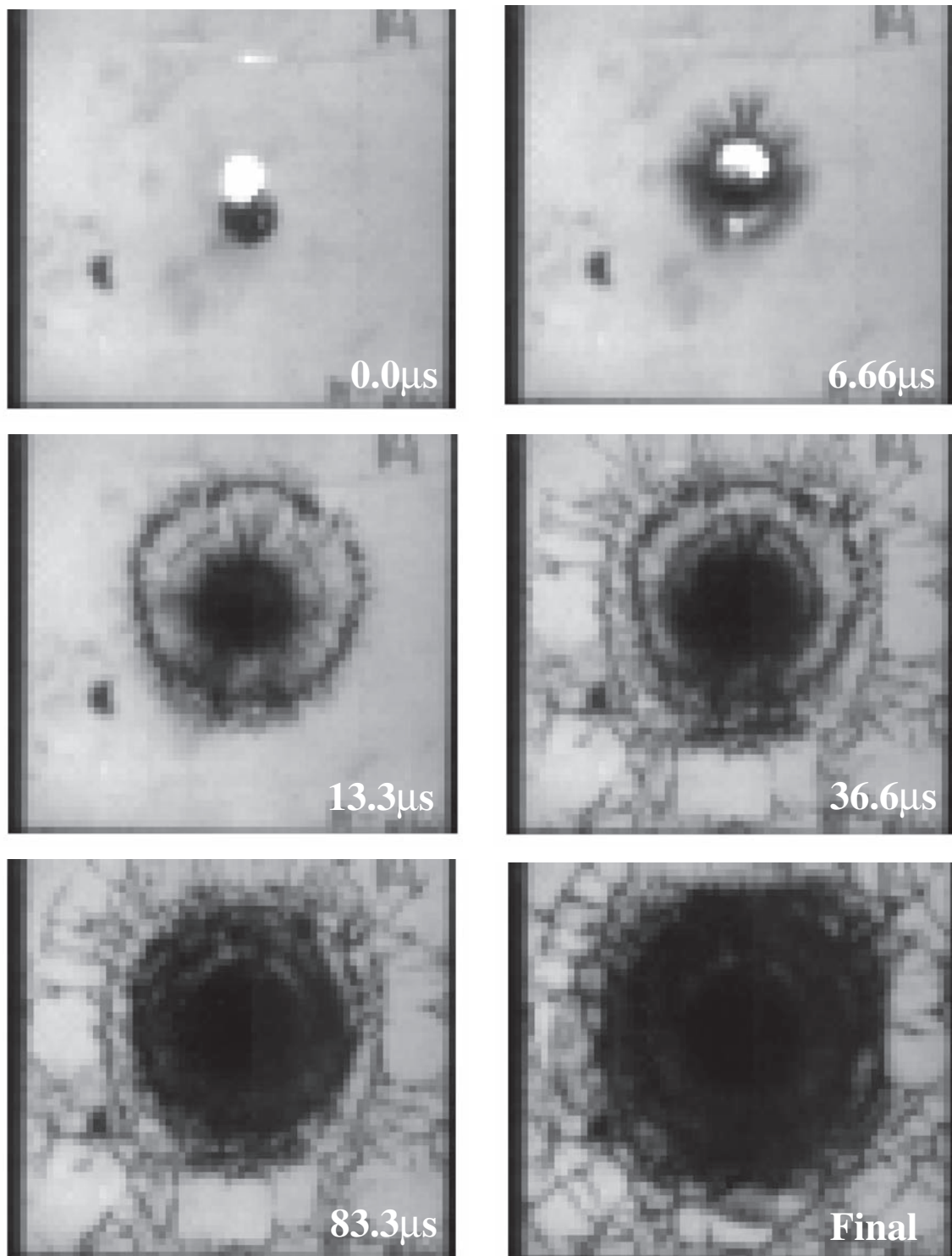


Fig. 8 Temporal evolution of damage in a 3.18-mm thick borofloat glass plate bonded to a 3.18-mm thick polycarbonate plate using a 2.54-mm thick polyurethane interlayer. Projectile: $5.51 \times 5.51 \text{ mm}^2$ steel RCC, velocity = 596 m/s, and strike face = tin side

The data in Table 3 document the execution of the projectile velocity step-up procedure employed in this study totalling 28 test shots under various conditions. The first seven test shots (test numbers 1–7) were carried out using the BB projectile impacting

the 3.175-mm thick borofloat strike-faced targets under the following conditions: (a) five air-side shots were conducted within a projectile initial velocity range of 468–525 m/s and (b) two tin-side shots were conducted with a single recorded velocity of

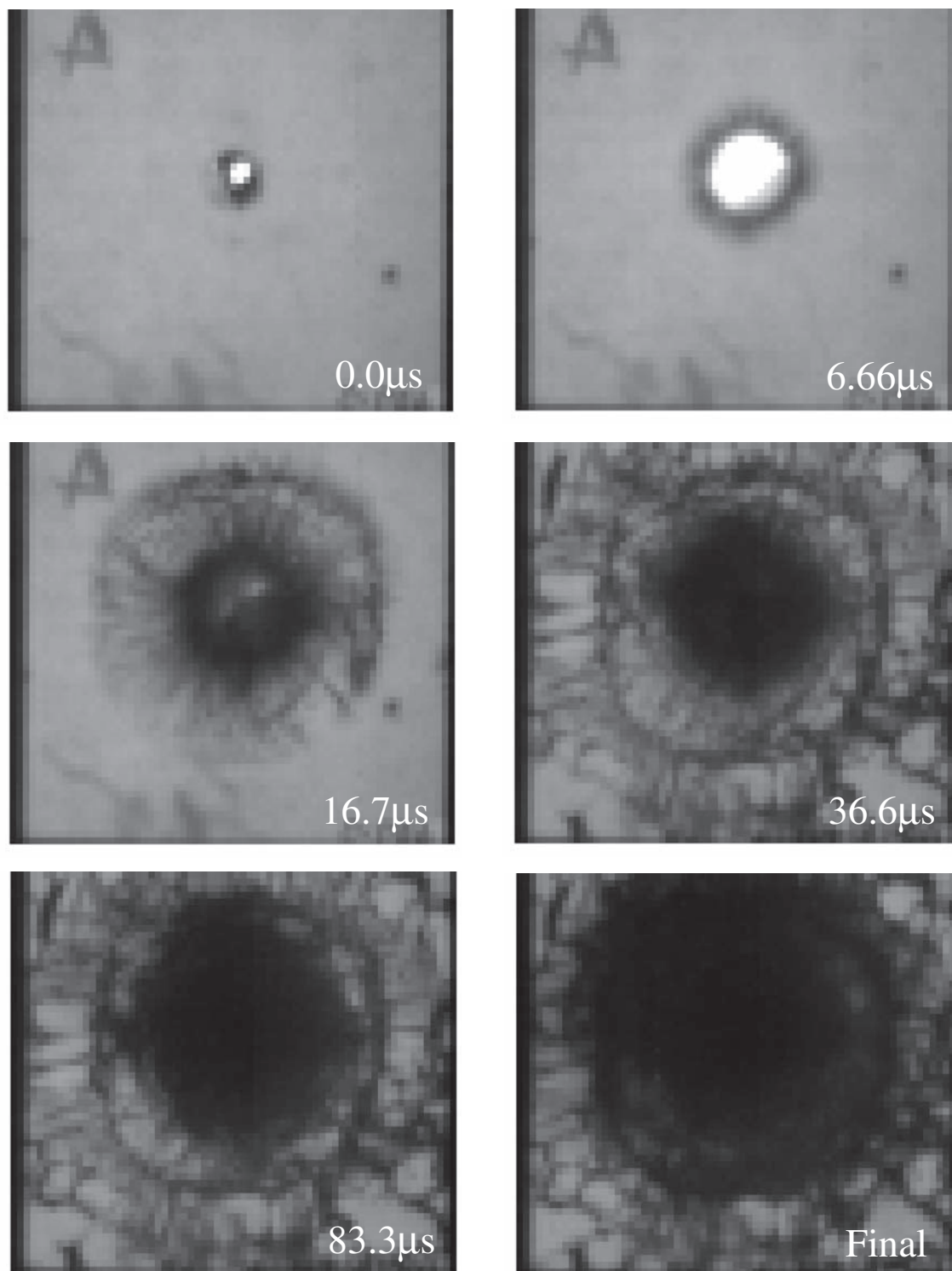


Fig. 9 Temporal evolution of damage in a 6.35-mm thick borofloat glass plate bonded to a 3.18-mm thick polycarbonate plate using a 2.54-mm thick polyurethane interlayer. Projectile: $5.51 \times 5.51 \text{ mm}^2$ steel RCC, velocity = 532 m/s, and strike face = air side

470 m/s and a subsequent errant velocity recording. It should be noted that any field containing the N/A symbol (such as this errant velocity recording) indicates a malfunction in some step of the test procedure; in this case, the side-mounted camera was not

triggered by the hand-operated switch. After seven shots, it was realized that the BB projectile was not able to perforate the target at the maximum pressure of the gas gun and the more massive RCC projectile was employed as a substitute. The subsequent 17

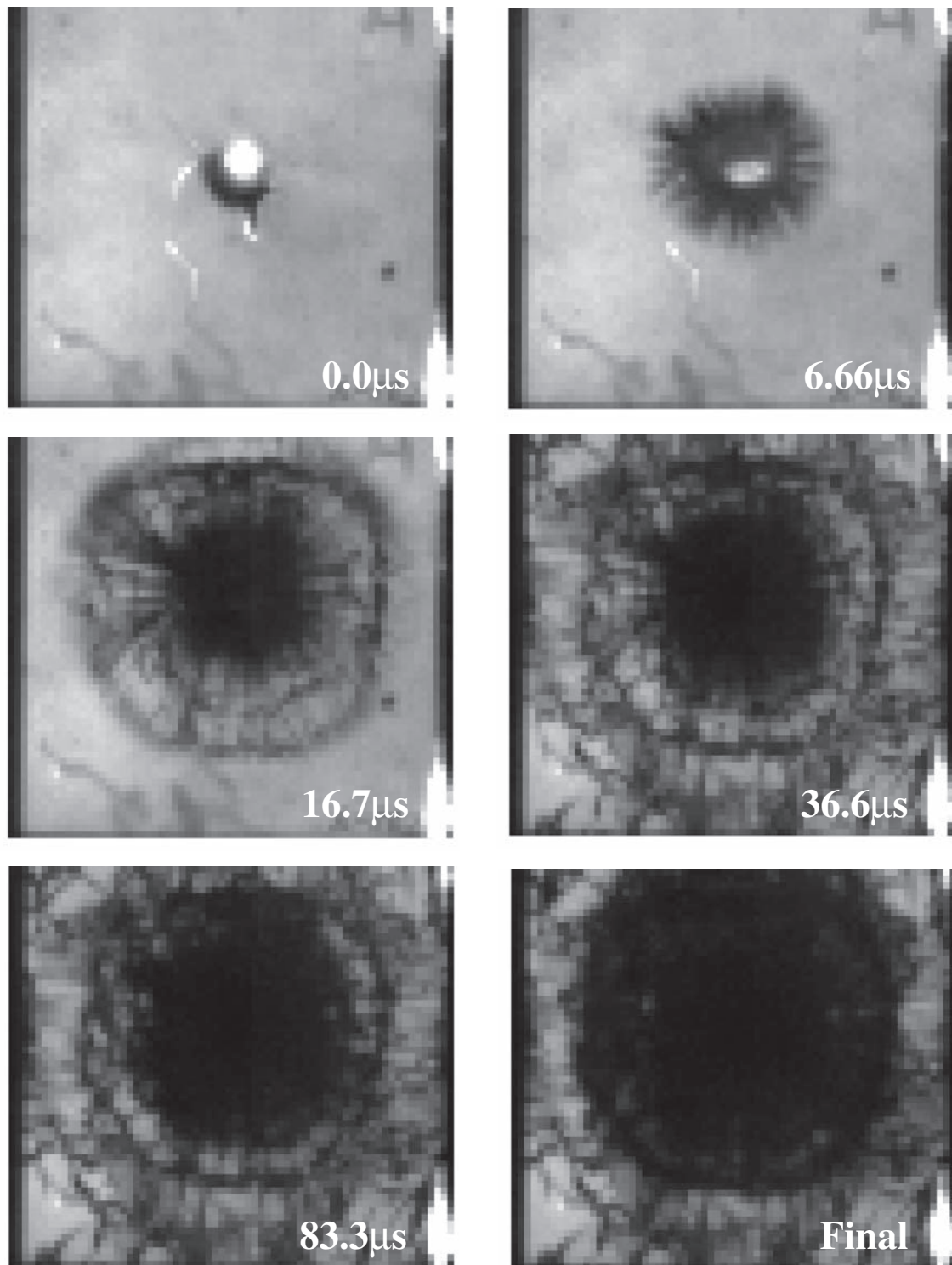


Fig. 10 Temporal evolution of damage in a 6.35-mm thick borofloat glass plate bonded to a 3.18-mm thick polycarbonate plate using a 2.54-mm thick polyurethane interlayer. Projectile: $5.51 \times 5.51 \text{ mm}^2$ steel RCC, velocity = 540 m/s, and strike face = tin side

shots (test numbers 8–24) were carried out using the RCC projectile impacting the 3.175-mm thick borofloat strike-faced targets under the following conditions: (a) ten air-side shots were conducted within a projectile initial velocity range of 391–547 m/s and

1 errant initial velocity recording and (b) seven tin-side shots were conducted within a projectile initial velocity range of 451–596 m/s. The final four shots (test numbers 25–28) utilized the 6.35-mm thick borofloat strike-faced targets under the following

conditions: (a) two air-side shots using the RCC projectile for the first and the FSP for the second where the initial velocities were 532 and 550 m/s, respectively; and (b) two tin-side shots both utilizing the RCC projectile with impact velocities of 380 and 540 m/s. It should be noted that the FSP was used on the last shot of the experiment when it was realized that the RCC was unable to perforate the thicker of the two targets; however, the FSP also proved to be incapable of target perforation. Table 3 also contains quantitative information regarding the impact coordinates of the projectile which quantify the degree to which a given shot was off-centre. The same eight test shots (test numbers 2, 3, 14, 15, 20, 23, 26, and 27) from the previous section were investigated and found to be off-centre (horizontally and or vertically) within a ca. 1–5 per cent range of the total target width.

The main post-impact quantities measured for the experiment including penetration status and accompanying residual velocities, dark-coloured region growth rate and its final diameter, and radial macro-crack growth rate are recorded in Table 4. The first set of results that were measured for all test shots is

Table 3 Experimental test conditions for the 28 test shots carried out on the transparent armour laminate structures

Test number	Strike face	Projectile	Impact velocity (m/s)	Impact coordinates (mm,mm)*
<i>3.18-mm thick glass</i>				
1	Air	BB	468	
2	Tin	BB	470	1.3,4.5
3	Air	BB	487	1.8,4.5
4	Air	BB	490	
5	Air	BB	525	
6	Tin	BB	N/A	
7	Air	BB	N/A	
8	Air	RCC	391	
9	Tin	RCC	451	
10	Tin	RCC	473	
11	Air	RCC	480	
12	Air	RCC	480	
13	Tin	RCC	490	
14	Tin	RCC	493	1.6,3.0
15	Air	RCC	493	5.8,4.7
16	Air	RCC	500	
17	Air	RCC	505	
18	Tin	RCC	521	
19	Air	RCC	526	
20	Air	RCC	540	3.8,4.0
21	Tin	RCC	540	
22	Air	RCC	547	
23	Tin	RCC	596	0.9,3.9
24	Air	RCC	N/A	
<i>6.35-mm thick glass</i>				
25	Tin	RCC	380	
26	Tin	RCC	540	3.1,8.3
27	Air	RCC	532	2.6,5.7
28	Air	FSP	550	

*0,0 corresponds to the centre of the glass plate.

related to the target perforation where the results are as follows: (a) zero of the seven test impacts utilizing the BB projectile leads to target perforation and hence are labelled as partial penetration (PP); (b) six of the ten air-side 3.175-mm thick glass strike face test shots yielded complete penetrations (CP) with target-exit residual velocities within a range of 0–106 m/s (with two errant residual velocity recordings). It should be noted that a CP is characterized by some amount of the projectile penetrating past the target back face (it is considered PP otherwise); thus, it is possible to have a CP with a residual velocity of 0 m/s if the RCC is partially stopped exiting the structure; (c) four of the seven tin-side 3.175-mm thick glass strike face test shots resulted in CPs with target-exit residual velocities within a range of 0–250 m/s; and (d) zero of the four 6.3-mm thick glass strike face test shots resulted in CPs.

The remaining results displayed in Table 4 were measured for the same eight representative test shots (test numbers 2, 3, 14, 15, 20, 23, 26, and 27) as the ones displayed in Figs 3 to 10. The first measurements pertain to the propagation speed of the dark-region damage front where the main findings are as follows: (a) all measured propagation speeds fell within a range of 135–148 m/s (a ~7 per cent difference); (b) there appears to be no discernable pattern in these velocities based on any of the following: projectile-type, target strike face, impact velocity, target-penetration status or glass strike face thickness. The corresponding results for the final diameter of the same dark-region damage zone can be summarized as: (a) the eight measurements fell within a range of 68–86 mm (~25 per cent difference); (b) the smallest two damage zones were associated with the two BB projectile test shots at 68 and 69 mm; (c) of the remaining six test shots that utilized the RCC projectile, the two smallest damage zones (78 and 72 mm) were associated with CP and high exit velocities while the other four were all associated with PPs or projectile yaw (i.e. the RCC longitudinal axis was not parallel with the strike face surface normal); and (d) there appear to be no further discernable patterns in these damage zone diameters based on any of the following: borofloat strike face, impact velocity, or glass lamina thickness. The final results quantified in Table 4 are concerned with the macrocrack propagation speed where the main findings are the following: (a) all measured macrocrack propagation speeds fell within a range of 2117–2282 m/s (a ~5 per cent difference); and (b) there, again, appears to be no discernable pattern in these speeds based on any of the following: projectile-type, borofloat strike face, impact velocity, target-penetration status, or glass lamina thickness.

Table 4 Experimental results of 28 test shots relative to penetration and damage evolution/distribution

Test number	Penetration status*	Residual velocity (m/s)	Dark-region growth rate (m/s)	Final dark-region diameter (mm)	Macrocrack speed (m/s)
<i>3.18-mm thick glass</i>					
1A	PP	0			
2T	PP	0	142	68	2120
3A	PP	0	143	69	2240
4A	PP	0			
5A	PP	0			
6T	PP	0			
7A	PP	0			
8A	PP	-17			
9T	PP [†]	0			
10T	PP	-9			
11A	CP	0			
12A	CP	0			
13T	PP	-5			
14T	CP	197	141	78	2151
15A	PP [†]	0	148	87	2129
16A	PP [†]	0			
17A	CP	106			
18T	CP	0			
19A	CP	0			
20A	PP [†]	-3	145	83	2196
21T	CP	0			
22A	CP	N/A			
23T	CP	250	145	72	2117
24A	CP	N/A			
<i>6.35-mm thick glass</i>					
25	PP	-14			
26	PP [†]	-12	135	85	2282
27	PP [†]	-12	141	86	2120
28	PP [†]	-12			

*PP, partial penetration; CP, complete penetration.

[†]Projectile yawed at time of impact.

5.1.3 Determination of V50

It should be recalled that the main objective of this study was to examine the effect of the air-side versus tin-side strike face orientation on the penetration resistance of the borofloat plate glass within a three-layer transparent armour structure. The results displayed in Figs 3 to 10 and Tables 3 and 4 and discussed in the previous two sections did not reveal any evidence of the effect of borofloat strike face selection on the nature and the kinetics of the prominent deformation/damage processes. In this section, an attempt is made to establish if this selection has an effect on the laminate penetration resistance as quantified by the V50. The first step towards determining the V50 was to use the results displayed in Table 4 to construct the corresponding projectile residual velocity versus projectile initial velocity plots for the air-side and tin-side-oriented borofloat strike faces. Since the results associated with the BB projectiles did not result in target penetration, they were not included. For the same reason, the results for the thicker borofloat laminates were also not considered. Thus, for the air-side case, results associated with test shots 7, 8, 11, 12, 15–17, 19, 20, and 22 were

used, while for the tin-side case the results associated with test shots 9, 10, 13, 14, 18, 21, and 23 were used. It should be noted that while computing the V50 values given above, the zero residual velocity CP results from Table 4 are treated as 'no penetration cases'. The resulting projectile residual velocity versus projectile impact velocity data scatter plots are shown in Fig. 11. The results displayed in this figure are used to determine the V50 as the arithmetic mean of the lowest projectile initial velocity at which full penetration occurs and the highest projectile initial velocity at which no penetration occurs. This procedure yields V50s of 515 and 516.5 m/s for the air-side and the tin-side-oriented strike faces, respectively. This finding suggests that borofloat strike face orientation selection does not have a statistically significant effect on the transparent armour laminate penetration resistance.

5.2 Computational results

Since the experimental results presented in the previous section suggested no statistically significant effect of borofloat strike face orientation on either the deformation/damage response of the borosilicate

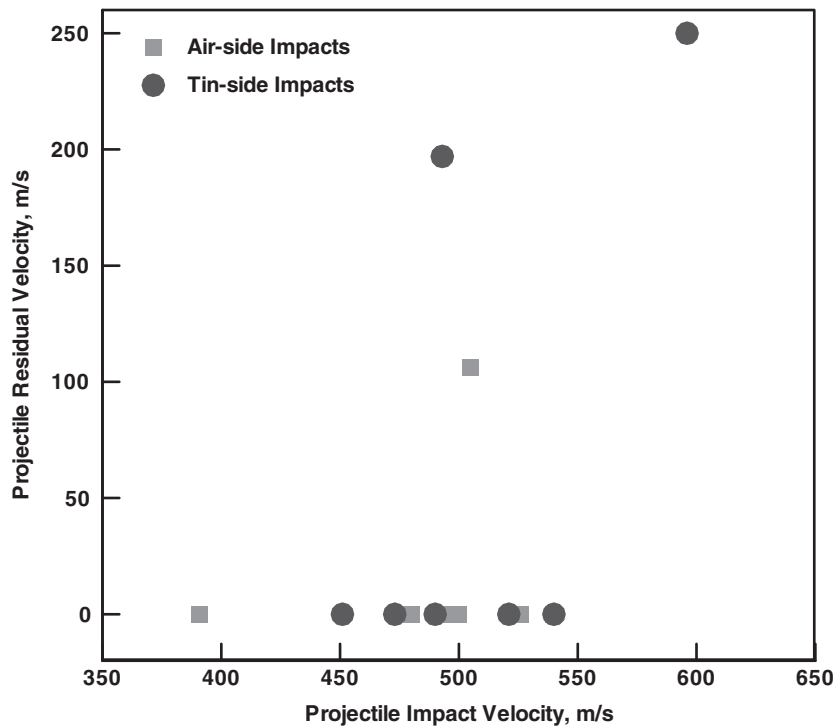


Fig. 11 Projectile residual velocity versus projectile initial velocity plot used to determine the air-side and tin-side strike-faced target V50s

lamina or the penetration resistance of the three-layer laminate, the main objective of the computational analysis was to: (a) reconfirm that borofloat strike face orientation has no first-order effect and (b) establish if the prominent experimentally observed damage modes and the measured V50 could be reproduced by the employed numerical analysis. For brevity, only ballistic impact scenarios associated with the RCC projectile and the 3.175-mm thick borofloat strike face laminates are considered in the remainder of this section.

5.2.1 The effect of borofloat strike face orientation

A comprehensive post-processing analysis of the computational results could not establish that air-side versus tin-side strike face orientation plays a statistically significant role on the ballistic response of the transparent laminate studied in this study. Hence, no distinction will be made between the air-side and tin-side-oriented strike faces in the remainder of this section.

5.2.2 Damage mode characterization

The experimental results reported in the previous section identify the following main damage modes within the borofloat lamina: (a) comminution/

coherent damage; (b) radially oriented discrete macrocracks; (c) ring-cracking; and (d) borofloat/polyurethane interfacial damage. The computational results below confirm the ability of the present computational approach to correctly predict the occurrence of these damage modes.

The computational results displayed in Fig. 12(a) show a top view of the quarter-model borofloat strike face laminate at the post-impact time of 8.0 μ s. In order to reveal the damage in the region underneath the projectile, the projectile is not displayed. For the same reason, the material having undergone complete coherent damage is not shown. Two of the previously identified damage modes (i.e. coherent damage and radial macrocracking) are evident in this figure. The coherent damage region is identified by the light-blue, green, and yellow elements corresponding to various degrees of coherent damage with the fully damaged material being removed from the display, while the macrocracked material is displayed in red.

The computational results displayed in Fig. 12(b) depict a top view of the quarter-model borofloat strike face laminate at the post-impact time of 16.0 μ s. Examination of this figure reveals that in addition to the aforementioned coherent and radial macrocrack modes of damage, a third mode (i.e. ring-cracking) has appeared.

The computational results obtained at later post-impact times revealed the onset of the fourth

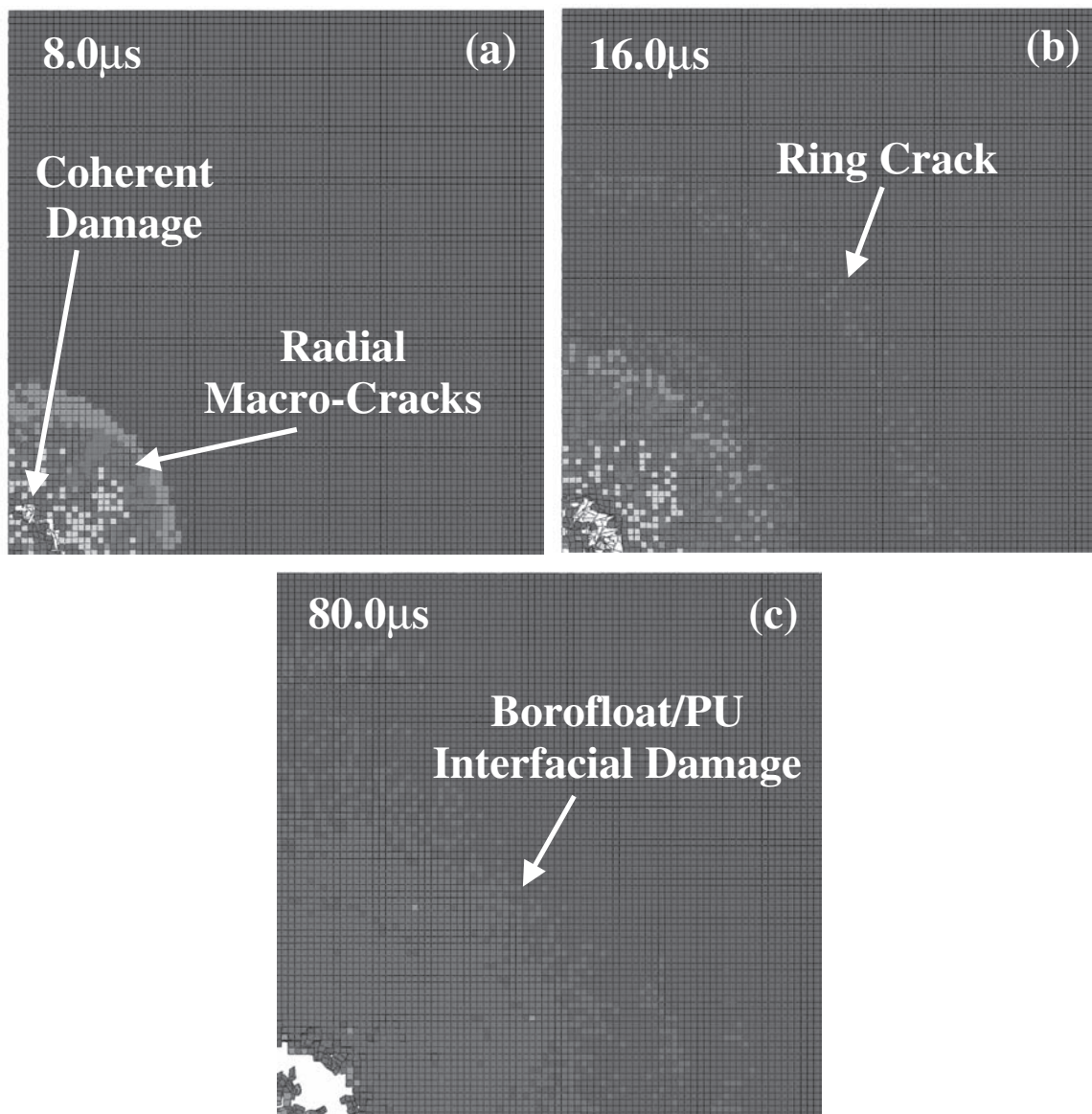


Fig. 12 Temporal evolution of damage resulting from the computational simulation of ballistic impact onto a 3.175-mm thick borofloat glass plate bonded to a 3.18-mm thick polycarbonate plate using a 2.54-mm thick polyurethane interlayer. Projectile: $5.51 \times 5.51 \text{ mm}^2$ steel RCC, velocity = 510 m/s, and strike face = air side

damage mode, i.e. borofloat/polyurethane interfacial damage. To show this damage mode, a bottom view of the quarter-model borofloat strike face laminate at the post-impact time of $80.0 \mu\text{s}$ is displayed in Fig. 12(c). It should be noted that in this figure, the polycarbonate and polyurethane laminae (in addition to the projectile) are not displayed.

5.2.3 Evolution kinetics and spatial distribution of damage

It should be recalled that the experimental results presented in the previous section yielded quantitative information regarding the dark-region growth rate

and its final size and the radial macrocrack propagation speed. It should also be recalled that the growth kinetics of the dark region was initially dominated by evolution of coherent damage and at later post-impact times was dominated by the borofloat/polyurethane interfacial damage progression. By subjecting the computational results to a post-process quantitative analysis, the following values were obtained for the damage-kinetics parameters: (a) dark-region growth rate 160 m/s; (b) dark-region final diameter 80–90 mm; and (c) radial macrocrack propagation speed 2410 m/s. The results are thought to be within reasonable agreement with their experimental counterparts reported in the previous section.

5.2.4 Determination of V50

By employing the same V50-determination procedure described in the section 4.1, mean values of the computational equivalent of this quantity were found to be 519 and 520 m/s for the air-side and the tin-side-oriented strike faces, respectively. Since these values are fairly close to their experimental counterparts (515 and 516.5 m/s), it is clear that the present computational model/analysis can reasonably well predict the penetration resistance of the three-layer transparent armour laminate.

5.3 General discussion

At the onset of the research, it was expected that orienting the borofloat tin-side as the strike face would improve the impact resistance performance of a glass-based transparent armour. This expectation was based on the observation that when testing individual glass plates that tin-side projectile impacts lead to ca. 3–5 per cent higher V50 values when compared to air-side impacts (i.e. enhanced ballistic protection performance) (B. Cheeseman, 2009, personal communication). However, such an increase in the ballistic protection performance was perceptible in neither the experimental nor computational components of this study. This does not mean that ballistic performance enhancement cannot be achieved by borofloat tin-side strike face selective orientation, but instead highlights the lack of such a response in the specific transparent laminate system and test conditions examined here.

Multiple contributions may have led to the nearly equivalent impact performance of the air-side and tin-side strike-faced borofloat transparent armour laminates. It is thought that the incorporation of borofloat into a laminate system has tempered/concealed the impact performance enhancement of the tin-side strike-faced borofloat lamina (the local effect) by additional system level effects. One effect is simply that with additional (polyurethane and polycarbonate) laminae, the impact performance enhancements of the transparent laminate obtained by optimizing a single (borofloat) lamina may be made insignificant, especially if that lamina is not the majority constituent (as is in the present case). Preliminary computational investigations in our ongoing work have indeed indicated that increasing the borofloat lamina relative thickness may lead to the occurrence of superior tin-side strike face ballistic protection performance of a three-layer transparent armour laminate. An additional system-level effect that is currently being investigated is the borofloat/polyurethane interface

decohesion (which is believed to be the source of the dark-region growth) to determine the degree to which this interaction contributes to the overall performance.

6 SUMMARY AND CONCLUSIONS

Based on the experimental and computational analyses of the air-side versus tin-side borosilicate strike-faced transparent armour laminate carried out in this study, the following main summary remarks and conclusions can be drawn.

1. Twenty-eight experimental test shots were carried out using three different projectiles and two thickness of borofloat glass with varying strike face (air-side and tin-side) orientations in a glass/polyurethane/polycarbonate transparent armour laminate.
2. Examination of the experimental results revealed no measurable difference between the air-side and tin-side strike face ballistic protection performance with respect to the character and kinetics of the main damage modes and the laminate penetration resistance (as quantified by the projectile critical velocity, V50).
3. Computational modelling of three-layer transparent armour laminate impacts employing the enhanced glass material model were carried out which reconfirmed the lack of air-side versus tin-side strike face ballistic protection performance.
4. Reasonable agreement with the experimental results proved that the enhanced borofloat material model is capable of capturing the main experimentally identified glass damage modes (and their evolution) in addition to the laminate V50.
5. It is postulated and early work indicates that a thicker borofloat strike face lamina will reveal a ballistic impact-performance enhancement when the borofloat tin-side is oriented as the laminate strike face.

FUNDING

The material presented in this paper is based on the work supported by the US Army/Clemson University Cooperative Agreements W911NF-04-2-0024 and W911NF-06-2-0042, and by the Army Research Office (ARO) research contract entitled Multi-length Scale Material Model Development for Armor-grade Composites, Contract Number W911NF-09-1-0513.

© IMechE 2012

REFERENCES

- 1 **Strassburger, E., Patel, P., McCauley, J. W., Kovalchick, C., Ramesh, K. T., and Templeton, D. W.** High-speed transmission shadowgraphic and dynamic photoelasticity study of stress wave and impact damage propagation in transparent materials and laminates using the edge-on impact method. In Proceedings of the 23rd International Symposium on *Ballistics*, Tarragona, Spain, 16–20 April 2007, pp. 1039–1047.
- 2 **Strassburger, E., Patel, P., McCauley, W., and Templeton, D. W.** Visualization of wave propagation and impact damage in a polycrystalline transparent ceramic-AlON. In Proceedings of the 22nd International Symposium on *Ballistics*, Vancouver, Canada, 14–18 November 2005, pp. 769–776.
- 3 **AMPTIAC.** Army materials research: transforming land combat through new technologies. *AMPTIAC Qtrly*, 2004, **8**(4), 132.
- 4 **Grujicic, M., Pandurangan, B., Coutris, N., Cheeseman, B. A., Fountzoulas, C., Patel, P., and Strassburger, E.** A simple ballistic material model for soda-lime glass. *Int. J. Impact Engng*, 2009, **36**, 386–401.
- 5 **Grujicic, M., Pandurangan, B., Bell, W. C., Coutris, N., Cheeseman, B. A., Fountzoulas, C., and Patel, P.** An improved mechanical material model for ballistic soda-lime glass. *J. Mater. Engng Perform.*, 2009, **18**, 1012–1028.
- 6 **Denoual, C. and Hild, F.** Dynamic fragmentation of brittle solids: a multi-scale model. *Eur. J. Mech. Solids A*, 2002, **21**, 105–120.
- 7 **Hild, F., Denoual, C., Forquin, P., and Brajer, X.** On the probabilistic and deterministic transition involved in a fragmentation process of brittle materials. *Comput. Struct.*, 2003, **81**, 1241–1253.
- 8 **Zijlstra, A. L. and Burggraaf, A. J.** Fracture phenomena and strength properties of chemically and physically strengthened glass. *J. Non-Cryst. Solids*, 1986, **1**(1), 49–68.
- 9 **Nghiem, B.** *Fracture du verre et hétérogénéité à l'échelle submicronique*. PhD Thesis, University of Paris, France, 1998.
- 10 **Yazdchi, M., Valliappan, S., and Zhang, W.** A continuum model for dynamic damage evolution of anisotropic brittle materials. *Int. J. Numer. Methods Engng*, 1996, **39**, 1555–1583.
- 11 **Espinosa, H. D., Zavattieri, P. D., and Dwivedi, S. K.** A finite deformation continuum/discrete model for the description of fragmentation and damage in brittle materials. *J. Mech. Phys. Solids*, 1998, **46**(10), 1909–1942.
- 12 **Zavattieri, P. D. and Espinosa, H. D.** Grain level analysis of crack initiation and propagation in brittle solids. *Acta Mater.*, 2001, **49**, 4291–4311.
- 13 **Camacho, G. T. and Ortiz, M.** Computational modeling of impact damage in brittle materials. *Int. J. Solids Struct.*, 1996, **33**(20–22), 2899–2938.
- 14 **Howes, V. R.** Surface resistance to damage of the 'Tin Side' and the 'Air Side' of commercially produced thermally toughened and untoughened float glass. *J. Am. Ceram. Soc.*, 1978, **56**(11), 1049–1060.
- 15 **Wereszczak, A. A., Johanns, K. E., Kirkland, T. P., Anderson, C. E. Jr., Behner, T., Patel, P., and Templeton, D. W.** Strength and contact damage responses in a soda-lime-silicate and a borosilicate. In The 25th Army Science Conference, Orlando, FL, 27–30 November 2006, pp. 1–8.
- 16 **Krohn, M. H., Hellmann, J. R., Shelleman, D. L., and Pantano, C. R.** Biaxial flexure strength and dynamic fatigue of soda-lime-silica float glass. *J. Am. Ceram. Soc.*, 2002, **85**(7), 1777–1782.
- 17 **Nie, X., Chen, W. W., Wereszczak, A. A., and Templeton, D. W.** Effect of loading rate and surface conditions on the flexural strength of borosilicate glass. *J. Am. Ceram. Soc.*, 2009, **92**(6), 1287–1295.
- 18 **Pilkington, L. A. B.** The float glass process. *Proc. R. Soc. Lond. A Math. Phys. Sci.*, 1969, **314**, 1–25.
- 19 **Krohn, M. H., Hellmann, J. R., Mahieu, B., and Pantano, C. R.** Effect of tin-oxide on the physical properties of soda-lime-silica glass. *J. Non-Cryst. Solids*, 2005, **351**, 455–465.
- 20 **Grujicic, M., Pandurangan, B., Coutris, N., Cheeseman, B. A., Fountzoulas, C., and Patel, P. A.** Computational investigation of the multi-hit ballistic-protection performance of laminated glass-poly-carbonate transparent armor systems. *J. Mater. Engng Perform.* 2011. DOI: 10.1007/s11665-011-0004-3.
- 21 **Grujicic, M., Pandurangan, B., Coutris, N., Cheeseman, B. A., Fountzoulas, C., Patel, P., and Strassburger, E.** A ballistic material model for Starphire[®], a soda-lime transparent-armor glass. *Mater. Sci. Engng A*, 2008, **491**, 397–411.
- 22 **ABAQUS version 6.9, User Documentation, Dassault Systems**, 2009.